SIGNAL PROCESSING APPROACHES FOR SENSITIVE AND EFFICIENT

MEASUREMENTS OF STRUCTURES AND VIBRATIONS WITH AN OPTICAL

COHERENCE TOMOGRAPHY BASED VIBROMETRY SYSTEM, AND ANALYSIS OF

EFFECTS OF NOISE AND AN ADJACENT REFLECTOR ON THE MEASUREMENT

A Dissertation

by

SANGMIN KIM

Submitted to the Office of Graduate and Professional Studies of
Texas A&M University
in partial fulfillment of the requirements for the degree of

DOCTOR OF PHILOSOPHY

Chair of Committee,	Brian Applegate
Committee Members,	Javier Jo
	Kristen Maitland
	Jim Ji
Head of Department,	Mike McShane

August 2019

Major Subject: Biomedical Engineering

ABSTRACT

Optical Coherence Tomography (OCT) has been used extensively for many fundamental research and clinical applications since it provides cross-sectional images with high resolution non-invasively. Moreover, phase-sensitive OCT (PhOCT) technique makes OCT more appealing by producing functional information such as blood flow, elastic properties, and vibrational information. Among them, we are interested in measuring vibration to investigate functions of the middle and inner ear.

OCT based vibrometry has been explored using a swept-laser source because of its advantages in acquisition rate and imaging depth compared to an OCT system using a spectrometer. However, a swept-laser source carries inter- and intra-sweep variability which is a critical problems that negatively affects image quality and displacement sensitivity. Also, OCT vibrometry is vulnerable to a significant increase in processing time because of the considerable amount of data as well as longer processing steps that are required to obtain structural and vibrational information. Longer processing time can make OCT vibrometry less appealing to biologists and clinicians even though it provides useful information because of greatly reduced experimental and diagnostic throughputs. Finally, a theoretical framework has not been established to analyze the effects of additive noise or an adjacent reflector, either of which is intrinsic in OCT vibrometry, on vibratory measurements. Without this framework it is hard to evaluate the performance of a OCT vibrometry system and figure out methods to alleviate those negative effects. Therefore, we proposed methods in this work to solve these important issues that impede the progress in the use of swept-laser OCT based vibrometry.

The first problem, intrinsic in a swept-laser source, was tackled by a signal processing approach that calibrated every sweep of the laser with a complex FIR filter and interpolation. In this approach, a complex FIR filter was adopted to extract the non-linear wavenumber from a reference signal in an effective way, and interpolation was employed to calibrate OCT signals to have the same linear wavenumber for removing intra- and inter-sweep variability. For real time processing,

the proposed method was implemented on FPGA. This approach was compared to the traditional IFFT-FFT based spectral calibration and showed the use of less resources in FPGA and as good or slightly better OCT image quality and displacement sensitivity. Also, it was explored to compensate chromatic variation from a laser source with the complex FIR based approach. Results demonstrated that this method could correct the variation in real time. Therefore, they suggest its usefulness to calibrate sweep and power variation for a swept-laser.

The second problem was addressed by proposing an efficient acquisition scheme and implementing required processing steps on GPU. By combining these two methods, new M-scan data can be acquired through the Alazartech card while transferring and processing the previous one. This acquisition-processing scheme allowed a series of M-scan data to be acquired and processed in near real time, showing only a little latency slightly less than acquisition time. Also, this proposed scheme was applied to perform single point M-scan, BM-scan, and volume M-scan in order to obtain additional vibrational information as well as structures at one axial point (z-axis), over two dimension (x, z), and over three dimension (x, y, z), respectively. Therefore, it can allow biologists and clinicians to obtain structural and vibrational information quickly.

To tackle the last problem, the effects of additive noise and an adjacent reflector were derived in a way that they are separated from an ideal vibrational signal that does not have those effects. This separation permitted to theoretically figure out how additive noise and an adjacent reflector affect measuring vibrational amplitude and phase in frequency domain. The derived equations were verified with MATLAB simulation and then with a piezo electric element using a swept-source OCT system. It was shown that results from derived equations matched well with those from experiments. Also, methods to reduce those effects were discussed based on the derivation. Therefore, the proposed derivation can be used not only to evaluate the performance of an OCT vibrometry system, but also to find methods to alleviate the effects.

DEDICATION

I dedicate this dissertation to my wife, Jungsim and my son, Hajin who have supported me

throughout this long journey.

CONTRIBUTORS AND FUNDING SOURCES

Contributors

This work was supported by a dissertation committee consisting of Dr. Brian Applegate (advisor), Dr. Javier Jo, and Dr. Kristen Maitland of the Department of Biomedical Engineering and Dr. Jim Ji of the Department of Electrical Engineering.

A proposed calibration method in Chapter 3 was implemented on FPGA by Patrick Raphael, a software engineer in Dr. John Oghalai's group from the Department of Otolaryngology in University of Southern California. In Chapter 4, initial python codes used in a host computer was created by Patrick Raphael and initial GPU code to process M-scan data was by Dr. Scott Mattison, a former graduate student in Dr. Brian Applegate's lab.

Funding Sources

NOMENCLATURE

AC	Alternating Current
ADC	Analog to Digital Converter
CORDIC	COordinate Rotation Digital Computer
DC	Direct Current
DFT	discrete Fourier transform
DLL	Dynamic Link Library
FBG	Fiber Bragg Grating
FDOCT	Fourier Domain OCT
FFT	Fast Fourier Transform
FIR	Finite Impulse Response
FPGA	Field Programmable Gate Array
FWHM	Full Width at Half Maximum
GPU	graphic processing unit
IFFT	Inverse Fast Fourier Transform
LPF	Low Pass Filter
OCT	Optical Coherence Tomography
PDF	Probability Density Function
PhOCT	Phase-sensitive OCT
RIN	Relative Intensity Noise
RMS	Root Mean Square
SDOCT	Spectral-Domain OCT
SIMD	Single Instruction Multiple Data

SNR	Signal to Noise Ratio
SPL	Sound Pressure Levels
SSOCT	Swept-Source OCT
TDOCT	Time Domain OCT
VOCTV	Volumetric Optical Coherence Tomography and Vibrometry

TABLE OF CONTENTS

LIST OF FIGURES

xii

xiii

LIST OF TABLES

xiv

1. INTRODUCTION

Optical Coherence Tomography (OCT) is a noninvasive imaging technique that can image the internal structures of a biological tissue in a cross-sectional plane by measuring backscattered light. These cross-sectional images are resolved highly with 1~10 μm owing to the use of broad bandwidth light sources. The ability to obtain cross-sectional images with high resolution enabled OCT to be used extensively for many fundamental studies and clinical applications. Moreover, OCT can produce vibrational as well as structural information of a sample with the help of the phase-sensitive OCT (PhOCT) technique, making it more attractive. This functional extension is called OCT vibrometry which has revealed new insights into functions of the middle and inner ear by simultaneously measuring structures and vibrations of said structures. [1, 2, 3].

However, there are some technical problems that hinder the progress in the field of OCT vibrometry. The first problem is related to inherent issues in using a swept-laser source. An OCT vibrometry system was mainly implemented with spectral-domain OCT (SDOCT) in the past [4, 5, 6]. This is because the sensitivity of vibration measurement is kept stable since there are no moving parts in SDOCT configuration. However, acquisition speed and imaging depth are limited with this method due to limited acquisition rate and roll-off inherent in a spectrometer. To avoid these problems, studies have been conducted to exploit swept-source OCT (SSOCT) because of its advantages [7, 8, 9, 10]. First, swept-laser sources provide faster sweep rate and long coherence length, increasing acquisition rate and imaging depth. In addition, the SSOCT configuration offers an opportunity to use a balanced detector by adopting a Mach-zehnder interferometer, improving signal to noise ratio (SNR). In spite of these advantages, SSOCT has intrinsic problems stemming from the use of a swept-laser source. These problems originate from mechanical tuning of the wavelength of a swept-laser, which negatively affects the quality of acquired images and the sensitivity of vibration measurement.

The second problem that an OCT vibrometry system has is an increase in processing time. This problem originates from the significant amount of required data. A volumetric structural

image requires three dimensions of data (x, y, k) where x and y are axes for lateral directions and k is wavenumber. Whereas, one more dimension of time is added to data for a volumetric structural and vibrational image. This time dimension comes from the M-scan used to measure the vibration of a sample at a fixed position. And the required number of scans for one M-scan varies depending on a measurement time and the sweep rate of an adopted swept-laser. For example, if we measure vibration for 10 ms at each lateral location and a 100 kHz swept-laser source is used, 1000 scans are required for one M-scan. This scales up the size of required data by one thousand compared to acquiring structural information only. Not only does the large increase in the amount of data contribute to prolonged processing time. The increased number of processing steps is also an important factor in prolonging the process. This is because deriving vibrational amplitude and phase requires extracting, unwrapping and Fourier transforming interferometric phases. Therefore, without careful implementation of post-processing, it can take a lot of time to acquire meaningful results from an experiment.

The third problem arises from additive noise and adjacent reflectors inherent in performing OCT vibrometry. They negatively affect measuring the vibrational amplitude and phase of a sample of interest, but their effects are not fully understood theoretically. For this reason, there are no current theoretical supports or criteria to find methods that reduce those inherent effects and evaluate the performance of an OCT vibrometry system.

These three problems were tackled in this work to advance an OCT vibrometry system. The first problem, inherent in a swept-laser source, was overcome by implementing an efficient wavenumber calibration algorithm on a field programmable gate array (FPGA) as explained in Chapter 3. The second problem, related to processing time, was tackled by controlling data acquisition in an efficient way and by implementing post-processing on graphic processing unit (GPU). Those efforts enabled real-time processing of acquired data to produce structural and vibrational images as described in Chapter 4. The third problem was dealt with thorough theoretical derivation for the effects of additive noise and an adjacent reflector. And the derivation was validated with MATLAB simulation and with experiments using a piezo electric element as detailed in Chapter 5.

2. BACKGROUND

2.1 Principles of OCT

2.1.1 Introduction

Optical Coherence Tomography (OCT) is a noninvasive imaging technique that can provide structural information over a lateral range along a few millimeters depth in biological tissues by measuring backscattered light. The combination of potential penetration and high resolutions of $1 \sim 10\mu$ from the use of broad bandwidth light sources allows OCT to be used for many fundamental studies and clinical applications.

OCT uses an optical interferometer to make an interferogram for detecting the backscattered light from a sample. An interferometer is composed of a light source, a reference arm, a sample arm, and a detector as shown in Fig. 2.1. Light travels from the source to a beamsplitter where it is separated into two paths; one path is the reference arm, and the other is the sample arm. The light reflected from the sample/mirror travels back down its respective path to the beam splitter where the light from each arm is recombined and, depending on the optical pathlengths of both paths, may interfere. This interference is then converted to an electrical signal by the detector.

In order to derive an interferogram analytically, the transmitted light wave from the light source is simply expressed as

$$E_{LS} = s(k, \omega)e^{j(kz - \omega t)} \tag{2.1}$$

where E_{LS} and s(k, ω) are the electric field and its amplitude function from the light source, respectively. s(k,ω) is the function of wavenumber $k = 2\pi/\lambda$ and angular frequency $\omega = 2\pi\nu$ where λ and ν represents the wavelength and the frequency of the light wave.

Assuming that the beamsplitter is wavelength-independent, has the power splitting ratio of 0.5 and one reflector is located at the sample arm, the reflected waves from both arms can be expressed
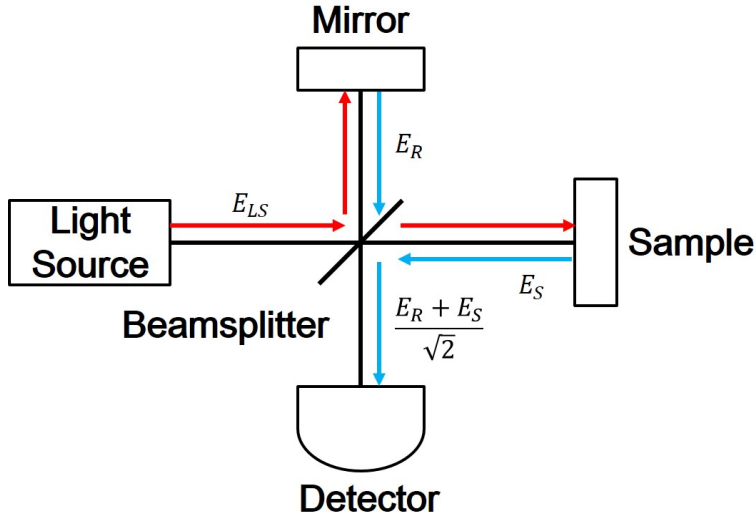
Figure 2.1: Michelson Interferometer in an OCT system. Red and Blue lines express incident and reflected light waves, respectively.

as

$$E_R = \frac{E_{LS}}{\sqrt{2}} r_R e^{j2kz_R}$$
$$E_S = \frac{E_{LS}}{\sqrt{2}} r_S e^{j2kz_S}$$

(2.2)

where E_R, r_R, and z_R are the reflected light wave, the reflectivity and the pathlength of the reference arm, respectively while E_S, r_S, and z_S are those of the sample arm. In Eq. (2.2), $\frac{1}{\sqrt{2}}$ term is multiplied because the light power is split in half at the beamsplitter. Also, the optical pathlength in each arm is doubled by the round trip of the wave.

Those reflected waves are combined at the beamsplitter and travel to the detector where they interfere and are converted to a photocurrent. Considering the responsivity of the detector, the

4

photocurrent can be express as

$$
\begin{aligned}
I(k) = \rho < \frac{|E_R + E_S|^2}{2} > &= \frac{\rho}{2} < |E_R|^2 + |E_S|^2 + E_R E_S^* + E_R^* E_S > \\
&= \frac{\rho}{4} < |E_{LS}|^2 R_R + |E_{LS}|^2 R_S + 2|E_{LS}|^2 \sqrt{R_R R_S}(e^{j2k(z_R - z_s)} + e^{-j2k(z_R - z_s)}) > \\
&= \frac{\rho}{4} < |E_{LS}|^2 R_R + |E_{LS}|^2 R_S + 2|E_{LS}|^2 \sqrt{R_R R_S} cos(2k(z_R - z_s)) > \\
&= \frac{S(k)}{4}(R_R + R_S + 2\sqrt{R_R R_S} \, cos(2k(z_R - z_s)))
\end{aligned}
\tag{2.3}
$$

where ρ is the responsivity of the detector, R_R and R_S are the power reflectivities of reference and sample arms, and S(k) is the power spectrum of the light source, meaning that $S(k) =< |s(k)|^2 >$. The angular frequency term $\omega = 2\pi\nu$ is removed in the final equation because the response time of a detector cannot keep up with the frequency of light (ν) due to its rapid fluctuation.

Assuming that S(k) is flat over the whole bandwidth, direct and alternating currents (DC and AC) are generated by interfering reflected waves as shown in Eq. (2.3). Also, it is found that the pathlength difference is encoded in the frequency of the alternating current. This implies that Fourier transform in k allows the sample reflectivity to be detected at the position of $2(z_r - zs)$ after the transform.

2.1.2 Fourier Domain OCT

Early OCT systems measured the sample reflectivity profile in z-domain like an ultrasound imaging modality. This technique is called time domain OCT (TDOCT) where one A-scan is measured by moving a reference arm mirror. However, it became possible to detect interferograms in Fourier (or wavnumber) domain as Fercher et al showed in [11]. This technique is called Fourier domain OCT (FDOCT) which allows one A-scan to be measured without moving the reference arm, significantly increasing imaging speed compared to TDOCT. It was also shown theoretically and experimentally that signal to noise ratio (SNR) of FDOCT was higher than that of TDOCT [12, 13, 14]. Therefore, these advantages of imaging speed and sensitivity led FDOCT to be a main technique in the field of OCT.

FDOCT can be classified by an optical configuration into two as depicted in Fig. 2.2: Spectral
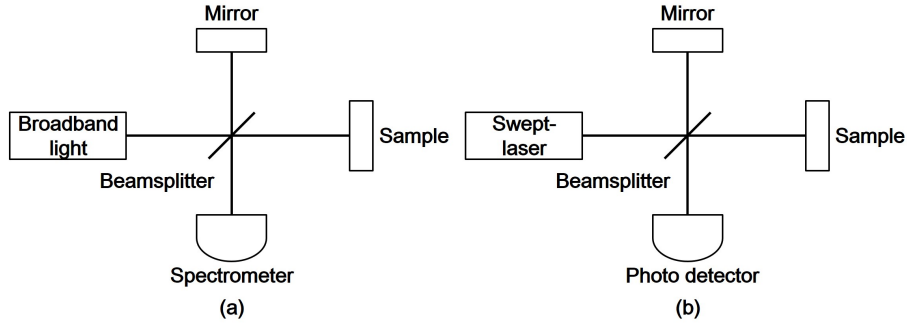
Figure 2.2: Optical configurations of (a) SDOCT and (b) SSOCT.

domain OCT (SDOCT) and Swept-source OCT (SSOCT). SDOCT uses a broadband light source and a spectrometer to detect interferograms along wavelength. In the spectrometer, light waves are divided by wavelength, thereby reducing light intensities before they hit a detector. This reduced light intensity causes decrease in shot noise because its standard deviation is proportional to the square root of light intensity. Thus, the use of the spectrometer allows sensitivity to be improved by reducing shot noise compared to TDOCT.

SSOCT adopts a swept-laser source where each wavelength of light is swept over time, and a photodetector is used to detect interferograms. Since each measurement time corresponds to an illuminated wavelength, this method allows us to detect interferograms in Fourier or wavelength domain. The sweep rate of a swept-laser source is generally faster than the acquisition rate of a spectrometer, which makes SSOCT faster than SDOCT. In addition, a balanced detector can be used in SSOCT by exploiting Mach–Zehnder interferometry. This balanced detection scheme cancels common mode noise and unwanted signals such as DC part and self-interference in a sample inherent in an interferogram [15]. Therefore, a higher SNR can be achieved with SSOCT compared to SDOCT. However, the mechanical tuning of a swept-laser negatively affects the performance of a system, requiring a careful calibration technique. The calibration technique will be explained in detail in Chapter 3.

2.2 Principles of functional vibratory measurement with OCT

Advances in OCT techniques have allowed vibrations to be measured on the order of tens of picometers, enabling many studies on middle and inner ear mechanics. The main technique to detect vibrations is phase-sensitive OCT (PhOCT) that exploits an interferometric phase.
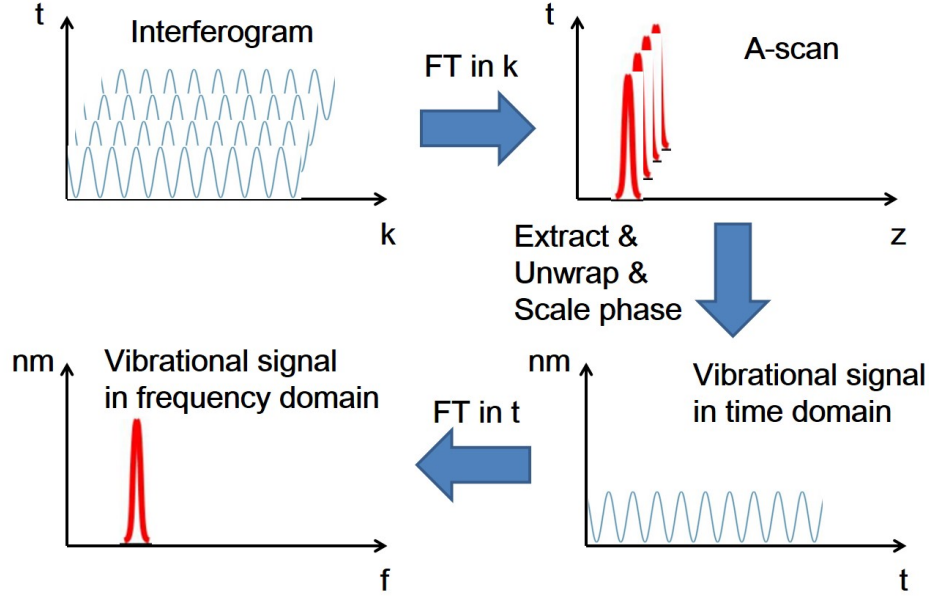
Figure 2.3: Phase sensitive OCT processing to acquire vibrational amplitude and phase from interferograms.

Obtaining vibrational amplitude and phase through PhOCT requires certain processing steps as described in Fig. 2.3. The first step is to acquire interferograms from a vibrating sample along time at a fixed position, which is called an M-scan. Assuming that there is one vibrating reflector and the DC part is removed, measured interferograms can be expressed as

$$I(k,t) = \frac{\rho S(k)\sqrt{R_R R_S}}{2}cos(2kn(\Delta z + \delta z(t))) = \frac{\rho S(k)\sqrt{R_R R_S}}{2}cos(2kn\Delta z + 2k_0 n\delta z(t)) \quad (2.4)$$

where t is time variable, Δz is the pathlength difference between reference and sample arms, $\delta z(t)$ is the subresolution displacement of a sample, and k_0 is the center wavenumber of a laser source.

Eq. 2.4 shows $\delta z(t)$ is encoded in the phase of the interferogram, implying $\delta z(t)$ should be decoded to derive the vibration of a sample. The next step is to generate A-scans by Fourier transforming the inteferograms.

$$i(z,t) = \frac{\rho\sqrt{R_R R_S}}{2}s(z \pm 2n\Delta z)e^{\mp j2k_0\delta z(t)} \tag{2.5}$$

where s(z) is equal to Fourier transform of S(k).

Then the inteferometric phase is extracted at the position of the reflector along time. This extracted phase is unwrapped to suppress abrupt phase jumps and converted to radian to distance by multiplying by $1/2k_0$ to have the unit of distance. From Eq. 2.5, the extracted vibrational signal can be expressed as

$$\frac{1}{2k_0}\angle i(2n\Delta z, t) = \delta z(t) = A_{vib}cos(2\pi f_{vib}t + \theta_{vib}) \tag{2.6}$$

where A_{vib}, f_{vib}, and θ_{vib} are vibrational amplitude, frequency, and phase, respectively.

As a final step, the time domain vibrational signal in Eq. 2.6 is transformed to the frequency domain.

$$\frac{1}{k_0}\angle i(2n\Delta z, f) = \delta z(f) = A_{vib}\delta(f \pm f_{vib})e^{\mp j\theta_{vib}}$$
$$\frac{1}{k_0}\angle i(2n\Delta z, f_{vib}) = \delta z(f_{vib}) = A_{vib}e^{j\theta_{vib}} \tag{2.7}$$

After the Fourier transform, the vibrational amplitude and phase are derived from the magnitude and the phase at the vibrational frequency as shown in Eq. 2.7. And they are used to provide functional information of a sample at the axial location where the time domain vibrational signal is extracted.

3. HIGH-SPEED SPECTRAL CALIBRATION BY COMPLEX FIR FILTER IN PHASE-SENSITIVE OPTICAL COHERENCE TOMOGRAPHY[*]

3.1 Introduction

There are a variety of extensions of Optical Coherence Tomography (OCT) that take advantage of the interferometric phase to garner additional information. Some example applications include the measurement of blood flow with Doppler OCT [16, 17, 18] and tissue mechanical properties with OCT elastography [19, 20]. In particular, we are interested in using a technique called Phase-sensitive Optical Coherence Tomography (PhOCT) to accomplish vibrometry with picometer sensitivities. This exquisite sensitivity is enabling 3-D vibrometry in the intact cochlea of animal models of hearing, revealing new insights into cochlea function. In recent work [2], we have quantitatively measured differential motion in the mouse Organ of Corti using techniques collectively called Volumetric Optical Coherence Tomography and Vibrometry (VOCTV).

PhOCT has most often been prosecuted with spectrometer based or Spectral-Domain OCT (SDOCT) systems owing to their inherent phase stability [4, 5, 6, 21, 22]. Nevertheless, there are several advantages to the swept-laser source or Swept-Source OCT (SSOCT) architecture. For example, swept laser sources typically have very narrow instantaneous line widths that provide long coherence length and therefore low sensitivity rolloff as a function of depth. Likewise, they are compatible with architectures using some variant of the Mach-Zehdner interferometer and balanced detection. Balanced detection cancels the DC part of the signal and suppresses common mode noise. Unfortunately, swept laser sources used for OCT typically suffer sweep instabilities that lead to phase noise and therefore reduced sensitivity.

Specifically, the mechanical wavelength tuning of the laser source causes the wavenumber to be swept nonlinearly and to vary within subsequent sweeps which are referred to as intra- and inter-sweep variability, respectively. Several hardware and software approaches have been proposed

to mitigate intra/inter-sweep variability. Postaid et al. and Choi et al. [7, 23] utilized a variable rate optical clock as a sampling clock for the Analog to Digital Converter (ADC) to remove intra-sweep variability. This method simplifies not only required hardware in the system but also the necessary post-processing. However, the ADC suffers from clock jitter generated by the variability of the optical clock. The clock jitter engenders a frequency dependent degradation of the signal-to-noise ratio (SNR) of the input signal [24]. Since the input signal is an interferometric signal, its frequency is a function of the optical pathlength difference. Therefore, the signal suffers more SNR degradation as the optical pathlength difference becomes larger, consequently deteriorating phase sensitivity as well as image intensity. There are software based approaches to deal with intra-sweep variability. Huber et al. [25] used a nearest-neighbor check algorithm to linearize the interferometric signal. This method is very efficient but not accurate. A more accurate algorithm was proposed by Gora et al. [8]. This method involves linearizing the interferometric signal using the phase of a reference interferometer. The phase of the reference interferometer is extracted by Fast Fourier Transform-Inverse Fast Fouirer Transform (FFT-IFFT) based Hilbert transform. This method is very accurate but requires substantial computation due to the FFT-IFFT process.

Several hardware based approaches have been used to remove inter-sweep variability. Vakoc et al. [26] and Baumann et al. [9] used a phase reference signal created by additional optics placed in the sample arm. The phase calibration signal is then used to measure and remove the inter-sweep variability. However, this approach requires careful adjustment so that the magnitude of the phase reference signal is sufficient for calibration but weak enough to avoid autocorrelation artifacts. A new type of hardware approach was proposed by Choi et al. [7]. The method places a Fiber Bragg Grating (FBG) in the optical system to act as a wavenumber reference signal. The inter-sweep variability is compensated by using the wavenumber reference signal. However, this method reflects some portion of the interferometric signal and needs careful selection and alignment of the FBG to work well. From the software point of view, the inter-sweep variability can be eliminated by a correlation method used by Braaf et al. [10]. In this method, two adjacent phases of k-clock signals are correlated with each other to calculate a shift magnitude. The shift magnitude is applied to the

secondly measured k-clock signal to remove variations between sweeps. This method does not need additional optical hardware but has a considerable computational load due to the calculation of correlation between two adjacent sweeps. In summary, hardware only based methods do not require significant post-processing but they increase hardware and alignment complexities and can be accompanied by unwanted artifacts or signal degradation. On the other hand, software based methods require considerable post-processing to guarantee accuracy and additional hardware to generate a reference interferometer signal, but they do not degrade the signal or introduce artifacts.

In our work which requires very high phase stability, we have adopted an approach similar to Gora et al. [8], where each sweep of the laser is calibrated by using a reference interferometer. The Hilbert phase of the reference interferometer is proportional to the instantaneous wavenumber of the laser and can be used to resample the interferometric signal such that δk is constant. However, the traditional Fast Fourier Transform-Inverse Fast Fourier Transform (FFT-IFFT) based Hilbert transform comes with considerable computational overhead. An alternative approach is to use a complex Finite Impulse Response (FIR) filter to extract the phase of the reference interferometer. The complex FIR filter is composed of two FIR filters used to generate an analytic signal [27]. The use of the FIR filter has the advantage of digital hardware efficiency compared to the FFT-IFFT method [28]. Other methods that have been utilized include the delay element and Hilbert FIR filter approach [29], and a bandpass and Hilbert FIR filter approach [30]. The complex FIR filter has been implemented in ultrasound imaging to detect the envelope of a beam formed signal and in OCT imaging to detect blood velocity [29, 30]. However, to the best our knowledge we present here the first application of the complex FIR filter to calibrate via a reference interferometer each sweep of a swept laser for SSOCT. We explicitly consider the accuracy of the phase of the different FIR based Hilbert transforms. In the context of PhOCT, we consider the impact of phase errors on phase noise. Furthermore we mitigate the computational load of the FIR filters by utilizing a field programmable gate array (FPGA) which can reduce processing time by working in parallel with the digitization [31]. Finally, we make use of the magnitude of the Hilbert transform to calculate an "ideal" window function, which allows us to carefully control the sidelobes of our axial point

spread function.

3.2 Method

3.2.1 Proposed architecture

The proposed architecture is composed of two parts: phase extraction and resampling (as shown in Fig. 3.1). The phase extraction part uses a complex FIR filter to make an analytic signal, and coordinate rotation digital computer (CORDIC) to calculate the phase of the analytic signal. CORDIC allows a simple and efficient hardware implementation by using shift and add operations to calculate trigonometric functions [32]. The resampling part linearizes an interferometric signal henceforth called the OCT signal, by linearly interpolating it with the extracted reference interferometer phase and a linearized phase.
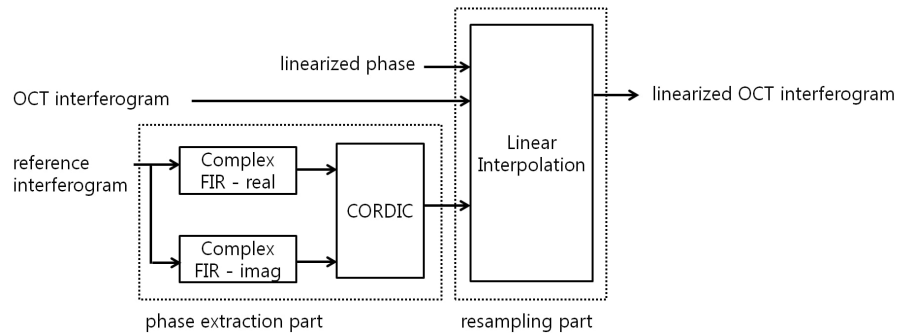
Figure 3.1: The proposed architecture for continuous real-time spectral calibration and linearization.

3.2.2 Generation and phase extraction of an analytic signal

The phase extraction from the reference interferometer is the most important task in the proposed architecture because it affects the accuracy of the spectral wavenumber calibration. Specifically, if the extracted phase has errors, those errors are propagated through the calculation of the depth resolved interferometric phase in the PhOCT image and reduces the system sensitivity. Therefore, it is important to extract the phase from reference interferometer accurately.

12

There are several types of FIR filter based methods for generating an analytic signal such as the delay element and Hilbert FIR approach, the bandpass and Hilbert FIR approach, and the complex FIR approach as shown in Fig. 3.2. Delay element and Hilbert FIR approach uses a delay element, Z^{-d}, for the in-phase signal to synchronize with the quadrature signal, and Hilbert FIR to make the quadrature signal. The bandpass and Hilbert FIR approach utilizes a bandpass FIR not only for synchronization but also for matching the bandwidth with the quadrature signal. The complex FIR approach consists of two filters: one from real coefficients, the other from imaginary coefficients. Ideally, these two filters exhibit an exact $\pi/2$ phase relationship as well as a matched frequency spectrum. The $\pi/2$ relationship is important for an analytic signal to be correctly defined as in Euler's formula. However, this property is not conserved in the other two FIR based methods, hence in this respect the complex FIR approach is the most accurate method among them.

In order to analyze and compare the FIR approaches mathematically, a reference interferometer signal was modeled using the following equation,

$$I_{RI} = \frac{\rho}{4}[s(k(n))(R_1 + R_2) + 2s(k(n))\sqrt{R_1 R_2}cos(2k(n)\Delta z_{RI})] \tag{3.1}$$

where n is the digital time index, k(n) is the wavenumber as a function of time, ρ is the detector responsivity, s(k(n)) is the power spectrum of the swept laser, Δz_{RI} is the optical pathlength difference in the reference interferometer, R_1 and R_2 are the reflectivities of the two arms of the interferometer. If we assume that the power spectrum is constant within the bandwidth, and $R_1 = R_2 = 1$, then Eq. (3.1) can be simplified to

$$I_{RI} = \alpha A + A cos(2k(n)\Delta z_{RI}) \tag{3.2}$$

where the constant A is equal to $\rho s(k(n))/2$, and α is a weighting factor less than 1 .
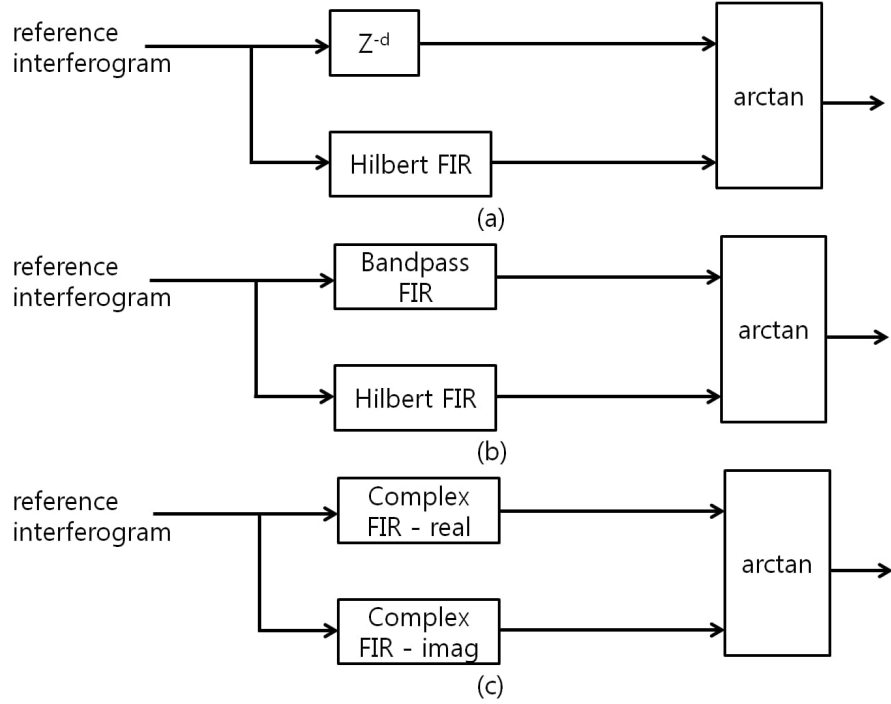
Figure 3.2: Block diagram illustrating several types of FIR filter approaches to generate an analytic signal (a): Delay element and Hilbert FIR approach (b): Bandpass and Hilbert FIR approach (c): complex FIR approach. In (a), Z^{-d} is a delay element to delay an input signal by d samples and Hilbert FIR is Hilbert transform implemented by FIR filter. The complex FIR filter has two kinds of filter coefficients: real and imaginary coefficients which are described as Complex FIR - Real and Complex FIR - Imag in (c), respectively.

Eq. (3.2) shows that the reference interferometer has both a bandpass signal and a DC signal. In principle, the DC signal is cancelled when a balanced detector is used. However, the imperfect spectral response of the fiber coupler and difference in responsivity of photodetectors in a balanced detector keep the DC signal from being removed completely. The imperfect DC cancelation is the origin of the parameter α. The DC component should be removed in order to extract the phase from the reference interferometer accurately.

Assuming the Hilbert FIR has no delay, the impulse response for the delay and Hilbert FIR approach in Fig. 3.2(a) can be expressed as

$$\delta(n) + jh_{Hilbert}(n) \tag{3.3}$$

14

where δ(n) is the impulse function and h$_{hilbert}$(n) is the impulse response of the Hilbert FIR filter. The analytic signal and its phase after going through the delay element and Hilbert FIR filter are then calculated as

$$(\alpha A + A cos(k(n)\Delta z_{RI})) * (\delta(n) + j h_{Hilbert}(n)) = \alpha A + A cos(k(n)\Delta z_{RI}) + j A sin(k(n)\Delta z_{RI})$$

with the corresponding phase

$$tan^{-1}(\frac{A sin(k(n)\Delta z_{RI})}{\alpha A + A cos(k(n)\Delta z_{RI})}) = tan^{-1}(\frac{sin(k(n)\Delta z_{RI})}{\alpha + cos(k(n)\Delta z_{RI})})$$

$$(3.4)$$

where $*$ denotes convolution.

As shown in Eq. (3.4), the DC component, αA, included in the reference interferometer signal is not removed by the delay element and thus ends up with the cosine term in the calculation of the arctangent and corrupts the phase estimation. On the other hand, the αA term is eliminated by Hilbert FIR filter whose magnitude response is characteristic of a bandpass filter. The bandpass and Hilbert FIR approach in Fig. 3.2(b) can overcome this issue and remove the DC component in the reference interferometer signal. Nevertheless it has an inherent phase error which prevents it from reproducing the correct π/2 phase relationship between the bandpass and the Hilbert FIR filters. That is,

$$H[h_{BPF}(n)] \neq h_{Hilbert}(n) \tag{3.5}$$

where H is the Hilbert Transform operator and h$_{BPF}$(t) is the impulse response of the bandpass FIR filter. The independent filter generation process for these two different FIR filters causes them to not have the correct π/2 phase relationship outside the passband region.

In contrast, the complex FIR approach in Fig. 3.2(c) generates real and imaginary filters dependently to ensure the exact π/2 phase relationship. In order to design the complex FIR filter, a low pass FIR filter (LPF) is designed first and then multiplied by a complex sinusoidal function. The resultant impulse response complex FIR filter can be expressed as

$$h_{LPF}(n)e^{-j2\pi f_0 n} = h_{LPF}(n)cos(2\pi f_0 n) - j h_{LPF}(n)sin(2\pi f_0 n) \tag{3.6}$$

15

where h$_{LPF}$(n) is the impulse response of the LPF.

As shown in Eq. (3.6), the real and imaginary filters have the same envelope, h$_{LPF}$(n) and the exact π/2 phase relationship. The analytic signal and its phase from the complex FIR approach are obtained using the appropriate h$_{LPF}$(n) and f$_0$ as

$$(\alpha A + A cos(k(n)\Delta z_{RI})) * (h_{real}(n) + jh_{imag}(n)) = A cos(k(n)\Delta z_{RI}) + jA sin(k(n)\Delta z_{RI})$$

$$with\ the\ corresponding\ phase$$

$$tan^{-1}(\frac{sin(k(n)\Delta z_{RI})}{cos(k(n)\Delta z_{RI})}) = k(n)\Delta z_{RI}$$

(3.7)

where h$_{Real}$(n) and h$_{Imag}$(n) are the impulse responses of real and imaginary filters for the complex FIR approach, respectively. As shown in Eq. (3.7), the phase is extracted without any artifact due to the DC component and with the exact π/2 relationship of real and imaginary filters.

3.2.3   Design of complex FIR filter

The proper selection of h$_{LPF}$(n) and f$_0$ is important to the design of the complex FIR filter. There are two approaches; a wideband complex FIR filter approach [27] and a narrowband complex FIR filter approach [30]. The wideband approach sets the passband of h$_{LPF}$(n) to be close to the normalized digital frequency of 0.25 and f$_0$ as 0.25. In the narrowband approach the passband of h$_{LPF}$(n) and f$_0$ are determined by the bandwidth and the center frequency of an input signal, respectively. Although the narrowband approach has better SNR by rejecting the out of band noise, it requires optimization for a given swept laser and reference interferometer. On the other hand, the wideband approach can cover the total frequency range even though it does not reject the out of band noise. The SNR of the reference interferometer signal tends to be high, hence the improved noise rejection in the narrow band case is not particularly helpful. We have chosen to take the wideband approach for our spectral calibration algorithm since a single set of filter parameters could readily work for multiple systems and is therefore more general.

In order to design the complex FIR filter, the prevalent Park-McClellan algorithm (equiripple design) was used. The specifications such as the passband and stopband frequencies (f$_p$ and f$_s$),

the passband ripple (δ_p), and the stopband attenuation (δ_s) are first determined. From them, a specification for $h_{LPF}(n)$ is developed by left-shifting the frequency response of the complex FIR by the normalized digital frequency of 0.25 as shown in Fig. 3.3.
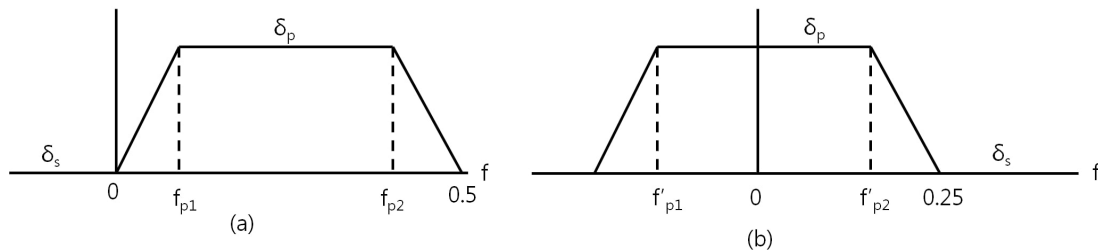
Figure 3.3: (a): The desired frequency response for complex FIR filter (b): The frequency response for the prototype LPF after left-shifting (a) by 0.25.

In the wideband approach, two stopband frequencies are easily defined as 0 and 0.5. Two passband frequencies are set as close to 0 and 0.5 as possible and should have the relationship between them of f_{p1}=0.5-f_{p2} in order to make $h_{LPF}(n)$ a real filter. However, getting closer to 0 and 0.5 requires greater filter length, incurring greater computational load and therefore hardware resources, Therefore, f_{p1} and f_{p2} are heuristically set to 0.1 and 0.4, respectively. In order to set (δ_s), the desired attenuation of the DC and the negative frequency component must be specified. Reilly et al. used the stopband attenuation of 0.17% below the passband [27]. By using this value, δ_s for both the DC and the negative frequency are reduced to 55 dB below the passband as depicted in Fig. 3.4. Fig. 3.4(a) shows the simplified frequency response of the reference interferometer from Eq. (3.2) where α is assumed to be 1 (worst case) generating a DC component 6dB higher than the frequency component of interest. Thus, δ_s is set to 0.085% (-61dB) in order to decrease the DC and the negative frequency components to -55dB and -61dB, respectively, as shown in Fig. 3.4(b). Since the equiripple design method requires the same ripples in both the passband and the stopband, δ_p is set as 0.085%. Using the stated filter specification and Kaiser's estimation method [33], the appropriate filter order was found to be 34.

17
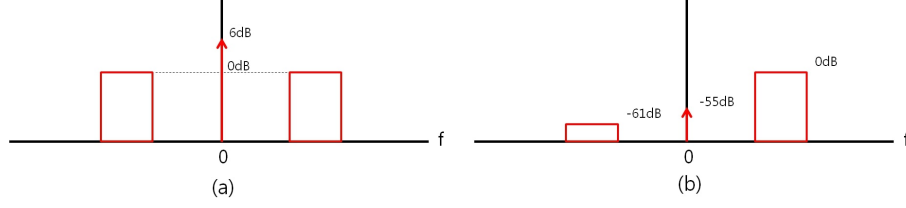
Figure 3.4: (a): The frequency spectrum of reference interferogram (b): the desired frequency spectrum of reference interferogram after complex FIR filtering.

3.2.4 Linearization of OCT signal

After extracting the phase from reference interferometer, the OCT signal is resampled such that δk is constant to enable the use of the fast Fourier transform. We have found that linear interpolation is sufficient for our purposes where we typically image near the zero pathlength difference. It is known that the performance of linear interpolation degrades as the depth approaches the Nyquist frequency, however the SNR is largely insensitive to the interpolation method [34]. The advantage of linear interpolation compared to polynomial interpolation methods is its computational simplicity. Assuming that the DC and auto-correlation terms of the signal are removed, the OCT signal for one reflector can be modeled as,

$$I_{OCT} = \frac{\rho}{2} s(k(n)) \sqrt{R_R R_S} \, cos(2k(n)\Delta z_{OCT})]$$ (3.8)

where Δz_{OCT} is the optical pathlength difference between the reference and sample arm of the OCT interferometer. Intersweep variability in k(n) leads to an apparent sweep to sweep change in the phase of the interferogram, i.e. the argument of the cosine in Eq. (3.8). Assuming a fixed number of samples are collected after the sweep trigger, this variability can also be thought of as a sweep to sweep change in the center frequency of the laser source. In order to mitigate this issue the interpolant was fixed and encompassed a range of k that was reliably spanned by each sweep of the laser. This approach fixes the beginning, ending, and center wavenumber of every sweep at a predetermined value, thus eliminating the associated phase error.

18

3.3 Results and Discussion

3.3.1 Simulation result

The performance of the FIR filter methods was first investigated by MATLAB simulation. For comparison, three FIR methods in Fig. 3.2 were designed with the same filter order of 34 and the same passband of 0.1 0.4. Fig. 3.5 shows the magnitude responses in the frequency domain of the three FIR approaches. Clearly, the DC component is not eliminated and the response is not flat in the negative frequency range for the delay element and Hilbert FIR approach, Fig. 3.5(a). Although the DC component is removed in the bandpass and Hilbert FIR approach, Fig. 3.5(b), the response is not flat in the negative frequency range. On the other hand, the complex FIR approach not only removes the DC component but also has flat magnitude response in the negative frequency range as depicted in Fig. 3.5(c). Errors in the estimation of the phase arise both from incomplete suppression of the DC component and residual negative frequency components.
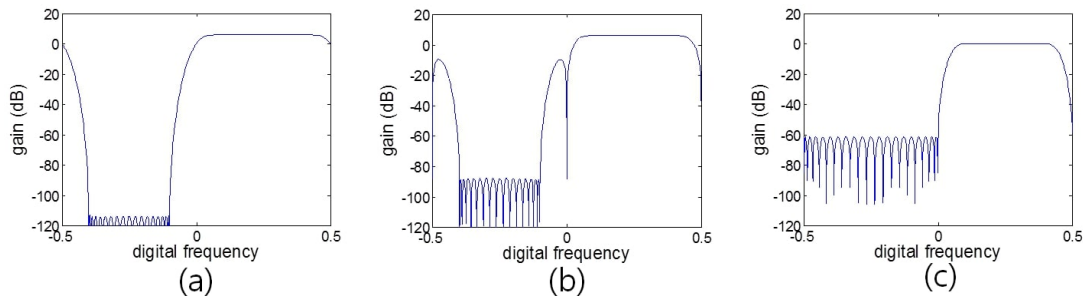
Figure 3.5: Frequency spetra of three FIR approaches. (a): delay element and Hilbert FIR filter (b): bandpass and Hilbert FIR filter (c): complex FIR filter

Next we compared the full calibration algorithm using the three different FIR approaches. Raw data was acquired from an OCT system with an identical architecture as [2] except the laser source had a 50 kHz sweep rate (SSOCT-1310, Axsun) and the digitizer was a 14-Bit, 250 MS/s Adapter Module (NI5761, National Instrument). The optical layout resembled a Mach-Zehdner interferometer with an optical circulator in the sample arm to preserve sample signal power. For additional

details on the hardware setup and signal processing steps see [2]. The raw data consisted of a set of 300 reference interferograms and the corresponding OCT interferograms that comprised an OCT B-scan image of a mouse cochlea. Fig. 3.6 shows the frequency spectra of reference interferograms filtered by delay element and Hilbert FIR, bandpass and Hilbert FIR, and complex FIR approaches as depicted in Fig. 3.6(c), (d) and (e), respectively. Each plot contains 300 reference spectral interferograms. The spectra processed with the delay element and Hilbert FIR approach, Fig. 3.6(c), and the bandpass and Hilbert FIR approach, Fig. 3.6(d), show a strong DC component and incomplete suppression of negative frequencies, respectively. In contrast, both DC and negative frequency components are eliminated in the complex FIR approach as seen in Fig. 3.6(e).
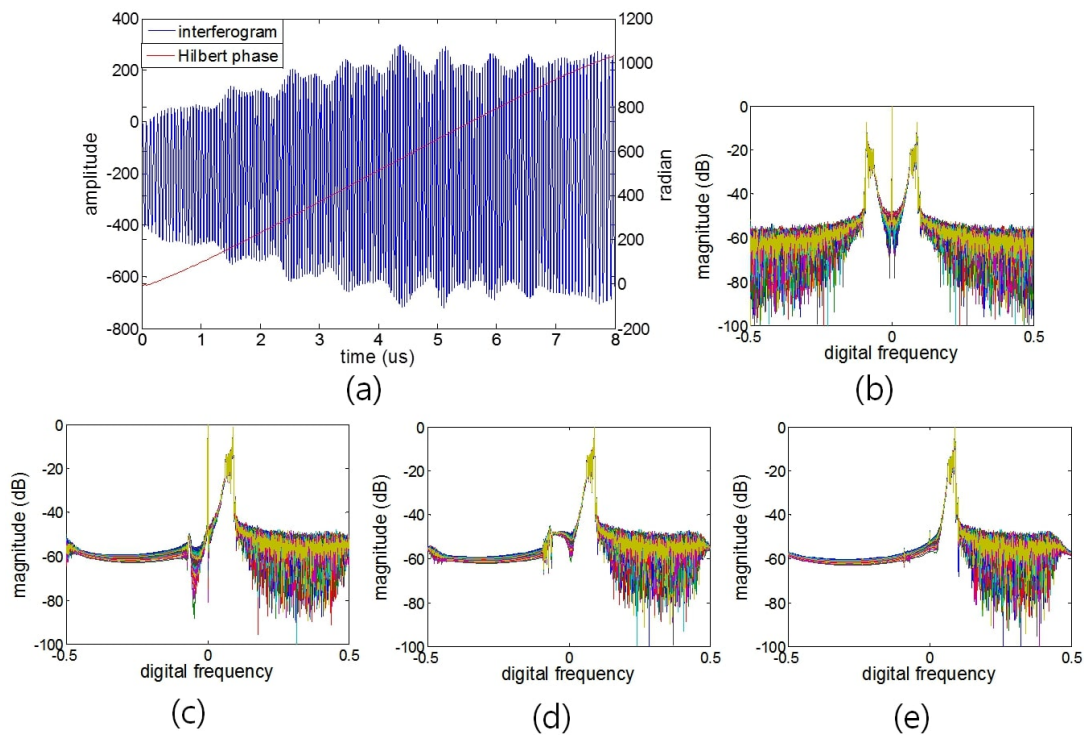
Figure 3.6: (a) Example reference interferogram overlaid with its Hilbert phase. The signal had a center frequency of 19.36 MHz and 0.0775 in digital frequency. (b) Reference interferograms in the frequency domain (c): filtered by delay element and Hilbert FIR approach (d): filtered by bandpass and Hilbert FIR approach (e): filtered by complex FIR approach. These spectra are obtained from 300 reference interferograms.

The B-scan images processed via the traditional FFT-IFFT approach and the three FIR approaches described here are shown in Fig. 3.7. The delay element and Hilbert FIR approach result in Fig. 3.7(b) shows strong ghost images repeated in depth which result from the high DC component as shown in Fig. 3.6(c). The bandpass and Hilbert FIR and complex FIR approaches (Fig. 3.7 (c) and (d)) show similar results that compared well to the traditional FFT-IFFT Hilbert approach (Fig. 3.7(a)). That is because the negative component is suppressed enough not to adversely affect the image in bandpass and Hilbert FIR approach. However, in principle the spectrum of the reference signal can be located at any frequency range. If the frequency of the reference interferometer falls in a range where the negative components are not well suppressed, artifacts will arise.
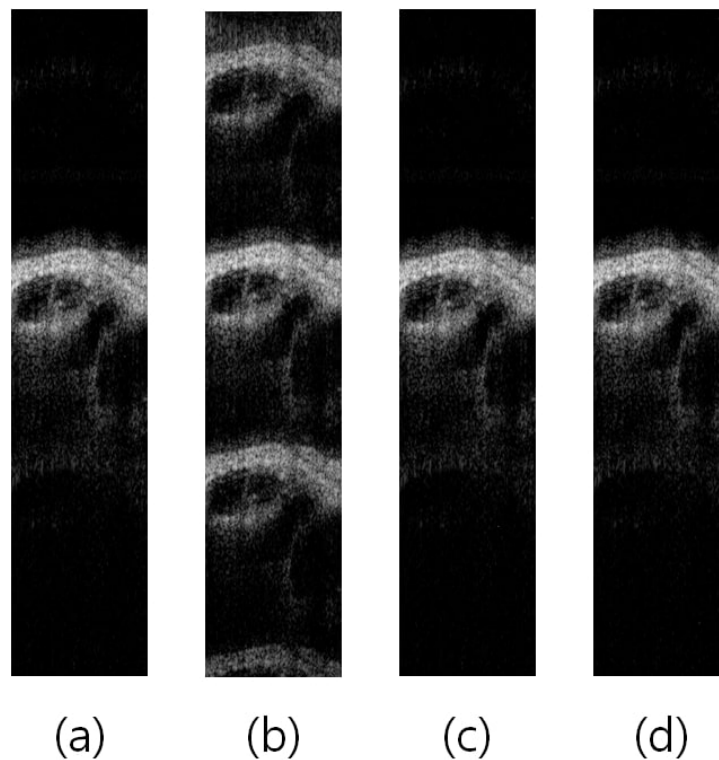
Figure 3.7: B-scan images of a mouse cochlea. (a): image from FFT-IFFT Hilbert transform (b): image from the delay element and Hilbert FIR approach (c): image from the bandpass and Hilbert FIR approach (d): image from the complex FIR approach. For reference the top of the images are near zero delay with digital frequency 0.024,and the bottom has a zero delay of 0.292.

21

For illustration, the unfiltered reference signal was shifted down by the normalized digital frequency of 0.03, and A-scans recomputed using the down-shifted reference signal. Fig. 3.8(a) shows the down shifted reference signal. Fig. 3.8(b) and Fig. 3.8(c) display the filtered signals by the bandpass and Hilbert FIR, and complex FIR approaches, respectively. Compared to Fig. 3.6(c) and Fig. 3.6(d), the negative frequency component is increased by about 20 dB for the bandpass and Hilbert FIR approach while it is essentially unchanged for the complex FIR approach. A-lines from the FFT-IFFT Hilbert Transform, bandpass and Hilbert FIR and complex FIR approaches are shown in Figs. 3.8(d)-(f), respectively. In the case of the bandpass and Hilbert FIR approach, strong artifacts arise at around 3.50 mm and 3.96 mm marked with an arrow in Fig. 3.8(e). These artifacts are not present in the result using the complex FIR approach which closely matches the result using the more traditional FFT-IFFT Hilbert transform.
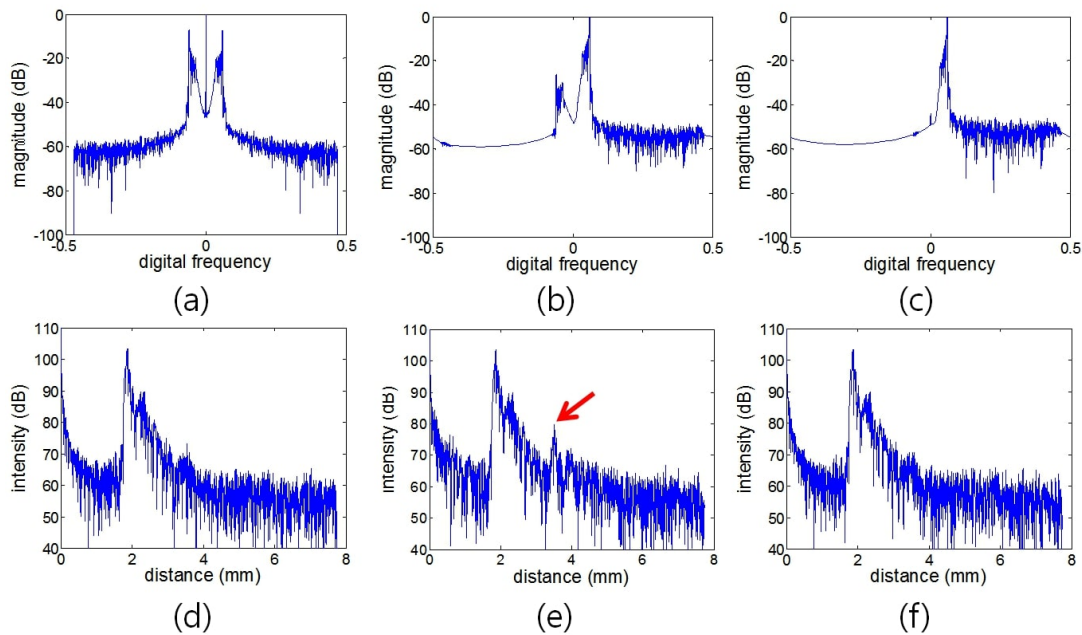
Figure 3.8: Effect of spectral down-shifting of the reference signal: frequency spectra of the down-shifted reference signal (a) before filtering, (b) bandpass and Hilbert FIR approach and (c) complex FIR approach. A-scans from (d) FFT-IFFT Hilbert transform, (e) bandpass and Hilbert FIR approach and (f) complex FIR approach. Red arrow indicates an artifact that arises due to incomplete suppression of the negative frequencies in the bandpass and Hilbert FIR approach.

In order to assess the different approaches for making vibratory measurements with PhOCT, we utilized a piezo electric element driven at 8 kHz. An M-scan consisting of 10000 A-scans was recorded and the data analyzed using each of the four approaches. The results are shown in Fig. 3.9.
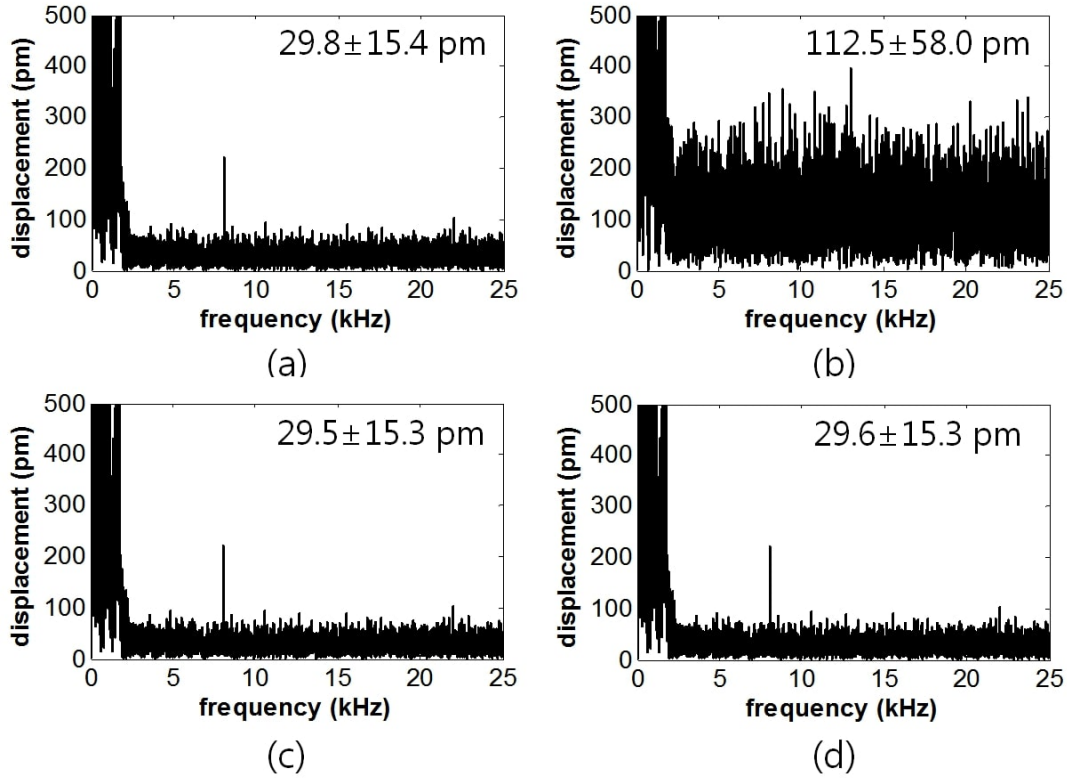
Figure 3.9: Frequency responses of displacement of a piezo, from (a) FFT-IFFT Hilbert transform (b) delay element and Hilbert FIR approach (c) bandpass and Hilbert FIR approach (d) complex FIR approach.

The phase noise of each approach is characterized by its mean $\pm$ standard deviation calculated in the range from 12.5 kHz to 25 kHz. The theoretical shot noise limited phase noise [35, 36] is 25.0$\pm$13.1 pm. The result from the traditional FFT-IFFT Hilbert transform, Fig. 3.7(a), showed a peak at 8 kHz with a magnitude of 221 pm and 29.8$\pm$15.4 pm phase noise. The result from the delay element and Hilbert FIR approach has no discernible peak and considerably worse phase

noise, 112.5±58.0 pm. The bandpass and Hilbert FIR and complex FIR approaches show similar results with a 221 pm magnitude peak at 8 kHz and 29.5±15.3 pm and 29.6±15.3 pm phase noise, respectively. As with the OCT B-scan image, the strong DC component in the delay element FIR approach severely compromises the results, however incomplete suppression of the negative frequencies in the bandpass filter FIR approach has no discernible impact. Based on the phase noise results both the bandpass and Hilbert FIR approach and complex FIR approach performed slightly better than the traditional FFT-IFFT Hilbert transform. The explanation lies in the difference in the number of data points of transient response between them. The FFT-IFFT Hilbert transform operation can be thought of as a circular convolution in the time domain with a FIR filter having the same length as the input signal [27]. Specifically, since we used 2000 data points per one reference interferogram, there were 1999 transient response data points for FFT-IFFT Hilbert transform while 34 points for bandpass FIR and complex FIR approaches. As a result, the FFT-IFFT Hilbert transform ends up with 1965 more unstable data points than the FIR approaches, which negatively affects the phase extraction of the reference signal. Presumably if we shifted the reference signal as in Fig. 3.7, the results from bandpass and FIR Hilbert approach would begin to deteriorate.

The bandpass and Hilbert FIR and complex FIR approaches provide comparable performance for both OCT imaging and OCT based vibrometry, at least to the limitations of the assessment presented here. Likewise, they have similar computational complexity. Nevertheless, going forward we have chosen to implement the complex FIR approach because it theoretically is more accurate, conserving the $\pi/2$ relationship between the complex components of the analytical signal, and completely suppresses the negative frequencies thereby mitigating potential problems related to the frequency of the reference interferometer signal.

3.3.2 FPGA implementation result

Our motivation for exploring the FIR approach to the Hilbert transform was to reduce the computational load from the traditional FFT-IFFT Hilbert transform. To that end, we have implemented the complex FIR approach on an FPGA and quantitatively compared the resource usage to our current FFT-IFFT method. The code was implemented on a Virtex-5 SX95T FPGA in an NI

24

PXIe-7965R with 18-bit precision. Table 3.1 shows device utilization for the FPGA implementing

post processing using the FFT-IFFT Hilbert and complex FIR approaches. The FFT-IFFT Hilbert

approach is based on the structure in Fig. 3.2(a) where the Hilbert FIR filter is replaced by FFT-

IFFT Hilbert transformation. The values in Table 3.1 include the operations in Fig. 3.2 as well as

linear interpolation and DC subtraction.   Since both sets of code were compiled with the same

Device Utilization	FFT-IFFT Hilbert approach	Complex FIR approach Score
Total Slices	90.3%	73.9%
Slice Registers	64.3%	43.4%
Slice LUTs	60.7%	42.1%
DSP48s	52.2%	33.4%
Block RAMs	36.5%	25%

Table 3.1: Comparison of device utilization of FPGA.

clock frequency, they output data at the same rate however the latency for the FIR approach is 17

clock cycles while that of the FFT-IFFT approach is 12,000 clock cycles. This difference is further

manifest in the resource usage. Since the complex FIR approach requires a smaller number of

additions and multiplications than the FFT-IFFT Hilbert approach, slice registers, slice LUTs and

DSP48s are reduced by around 20%. In addition, since the FFT-IFFT Hilbert approach requires

block RAM in order to match the latency between real and imaginary signals as in Fig. 3.2(a), the

usage of block RAM decreased by 11.5%. The results described here were for a system with a

200 kHz swept laser source. In order to test the implementation, a piezo was driven at 12 kHz

and its displacement was measured using a 200 kHz PhOCT system described in detail in [2]. The

displacement was measured 10 times with 4000 A-scans for each M-scan. Fig. 3.10 shows two

frequency spectra of the measured displacement: one using the FFT-IFFT Hilbert Transform and

the other from the complex FIR approach. The phase noise of each method was calculated as the

square root of an averaged noise energy in the frequency domain along the range of 20 kHz to 100

kHz. The result from the traditional FFT-IFFT Hilbert transform displays a peak at 12 kHz with a

magnitude of 3.78±0.06 nm and phase noise of 40.2±5.5 pm, where ± indicates the standard deviation among the 10 samples. The complex FIR approach showed similar results with a magnitude of 3.73±0.06 nm and 32.6±2.5 pm phase noise. In agreement with previous results, the complex FIR approach demonstrated slightly better phase noise than the FFT-IFFT Hilbert transform.
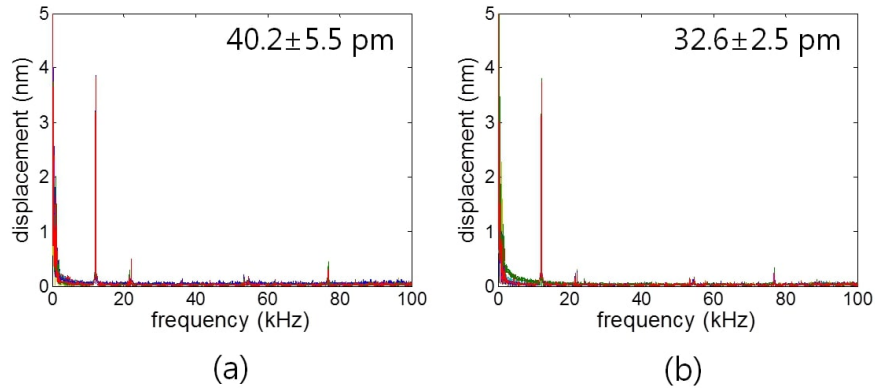
Figure 3.10: Frequency responses of displacement of a piezo, (a) from FFT-IFFT Hilbert transform (b) from complex FIR approach.

Reducing the number of coefficients used in the FIR filter can reduce the required resources. Owing to the fairly efficient multiply and addition operations on the FPGA, there is a limited potential for further gains over what we have shown in Table 3.1. Nevertheless, small reductions in the resources can be the difference between an FPGA code successfully compiling and not. In order to explore the limits we have experimented with how few coefficients could be used before the image quality and/or the phase sensitivity were compromised. We repeated the processing of the mouse cochlea and piezo using the complex FIR approach systematically reducing the number of coefficients while retaining the passband and stopband frequencies in order to only affect passband ripple and stopband atteunuation. Fig. 3.11(a) and Fig. 3.11(b)-(e) show phase noise and B-scan images at various filter orders, respectively. The phase noise was measured from filter orders ranging from 4 to 40 and quantified by the root mean square (RMS) in order to simultaneously consider mean and standard deviation. In Fig. 3.11(a), the phase noise converges to around 33

pm at the filter order of 8. The plateau above the order of 8 in Fig. 3.11(a) comes from the fact that the added noise caused by the complex FIR filter is below the system noise. The B-scan images were processed using the same filter orders as the phase noise measurement. Images using filter orders, 4, 8, 12 and 18 are displayed in Fig. 3.11(b)-(e), respectively. In these images there is clearly ghosting at the lower filter orders which essentially completely disappears with filter order of 18. These results taken together leads us to the conclusion that the filter order can be reduced to 18 without any noticeable impact. However, decreasing the filter order reduces the performance of the filter by increasing the passband ripple and the stopband attenuation if the passband and stopband frequencies are unchanged. Hence, careful selection of the minimum filter order is required, depending on the relative strength of the DC component to the frequency components in the reference interferogram.
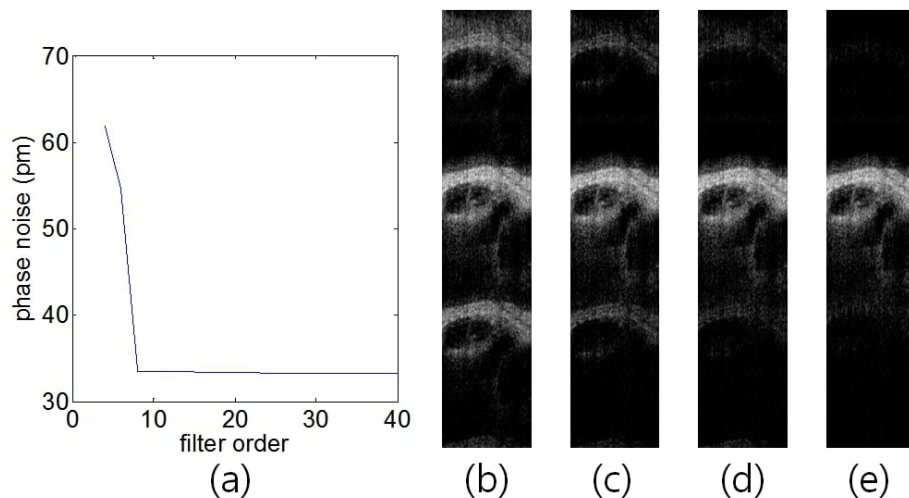
Figure 3.11: Phase noise and B-scan image in accordance with filter order. (a) shows phase noise calculated by Root Mean Square (RMS) according to the filter order ranging from 4 to 40. (b), (c), (d), (e) show B-scan images in accordance with the filter order of 4, 8, 12 and 18, respectively.

We have also explored the accuracy of the magnitude of the Hilbert transform, $|H|$, as a measure of the instantaneous swept laser power. We typically use this to calculate a custom window to be applied to the OCT spectral interferogram before computing the IFFT. The custom window

is meant to engender the spectral shape of a standard window function to the interferogram. For instance, if we desired the sideband structure of a Hanning window, we would calculate a custom window by $W_{cust}=W_{Hann}/|H|$. We do this to carefully control the sidelobe behavior of our axial point spread function. The phenomena of phase leakage [37] is well documented and known to cause errors in the estimation of depth resolved phase in OCT. Careful control of the sidebands can help mitigate this issue and reduce ambiguity in the interpretation of results of OCT vibratory measurements. Our standard procedure is to place a mirror reflector in the sample arm of the OCT interferometer, calculate the Hilbert transform of the OCT spectral interferogram and use the measured $|H|$ to calculate the W_{cust}. Since most swept laser sources have a relatively stable power and spectral shape at least after they have warmed-up we infrequently update this measurement. Therefore, our primary motivation was to determine if the complex FIR approach was accurate enough for this task in order to provide for simplicity and consistency in writing the code to run our system. Nevertheless, we recognized that there could be some advantage to recalculating the window for every sweep of the laser since any fluctuation in the laser power or spectral shape would automatically be compensated. Likewise, it would be a nearly trivial addition to the code already running on the FPGA if we could use the $|H|$ from the reference interferometer instead of a mirror reflector. In order to test this, the reflection from a mirror was measured using the 200 kHz PhOCT system. 12 M-scans were collected with 100 signal and reference interferograms. Among them, the first set of 100 A-scans was used to calculate dispersion compensation coefficients and a custom window using our standard procedure, as described above. Using this same set of data, coefficients to compensate for differences in chromatic losses between the signal and reference interferograms were calculated. In the proposed new algorithm, $|H|$ was calculated and then processed by low pass FIR filter (LPF) to remove additive noise before calculating the ideal window. The stopband of LPF was set to the normalized digital frequency of 0.05 because $|H|$ is a baseband signal with narrow bandwidth. We compared the new algorithm with and without correcting for chromatic losses to our current algorithm on the remaining 11 sets of data. Fig. 3.12 shows the results from one data set, in the depth range of the mirror reflection. The results were quantified

in terms of Full width at half maximum (FWHM) resolution, SNR and Main to Side lobe Ratio (MSR) for the 1st side lobes on either side. We found no difference for the FWHM resolution or SNR among the three algorithms. Specifically, the mean±standard deviation of the FWHM resolution over the 11 data sets was 8.56±0.18, 8.56±0.18 and 8.58±0.19 pixels, for the current method, without chromatic correction and with chromatic correction, respectively. The FWHM of the perfect Hanning window, W_{Hann}, was 8.38 pixels which compares well with the results obtained here with the custom window designed to impart the shape of a Hanning window to the interferogram. Similarly, the SNR was 61.47±1.76, 61.74±1.67 and 61.43±1.73dB, respectively. However, the MSR is degraded significantly if the chromatic correction is not included. From the data set in Fig. 3.12 the sidelobes increase by 1.85 dB and 3.44 dB. Likewise, it is fairly obvious in Fig. 3.12(a) that the sidelobe structure varies significantly when the chromatic correction is not applied. In contrast the sidelobe structure in Fig. 3.12(b) is faithfully reproduced even beyond the 1st sidelobes. These results indicate that the magnitude of the complex FIR Hilbert transform can be used to build a custom window and moreover it can be done using the reference interferometer as long as a chromatic correction is applied. We used a low-pass filter to suppress additive noise so that we could calculate a custom window on every sweep, however we found that using simple averaging of ~100 laser sweeps works equally as well if sweep to sweep variations are not a concern.
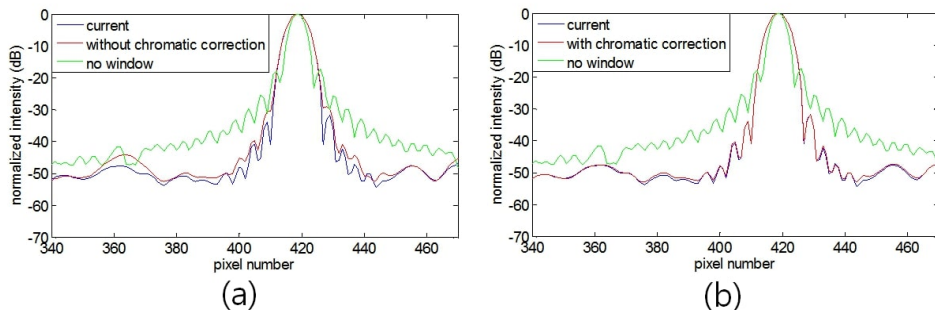
Figure 3.12: Comparison of methods for calculating a custom window. (a): axial point spread functions from current and proposed procedures without chromatic correction (b): axial point spread functions from current and proposed procedures with chromatic correction. For comparison, the axial point spread function with no windowing is also shown.

3.4 Conclusion

In this article we have evaluated several FIR based methods for spectral calibration of every sweep of a swept laser in real time. We found the complex FIR based approach was the most robust of the three considered. It provided as good or better results compared to the more traditional IFFT-FFT based Hilbert transform on OCT image quality and phase sensitivity. Our implementation on an FPGA also demonstrated that it used fewer hardware resources than the traditional IFFT-FFT approach. Our FPGA code used a filter order of 34 as recommended by Kaiser's estimation method. We also explored using lower filter orders and found that we could reduce the order to as low as 18 without impacting image quality and phase sensitivity. We also explored using the Hilbert magnitude of the reference interferometer signal as an instantaneous measure of the spectral power of the swept laser. We used this information to calculate an ideal window function that carefully controlled the sidelobes on the axial point spread function. We compared results derived from imaging a mirror with the OCT interferometer and an IFFT-FFT based Hilbert transform to those obtained from the reference interferometer and the complex FIR filter. We found that after a chromatic correction that accounted for differences in the wavelength dependent attenuation between the reference interferometer and the OCT interferometer, we were able to generate essentially equivalent results using both methods. However, the reference interferometer based measurement can be done in real time and is independent of the sample being imaged with the OCT interferometer. In conclusion, the complex FIR approach to the Hilbert transform allows for highly accurate real time wavelength and magnitude calibration of a swept laser source.

4. NEAR REAL-TIME VOLUMETRIC OPTICAL COHERENCE TOMOGRAPHY AND VIBROMETRY

4.1 Introduction

A vibratory measurement using OCT, called OCT vibrometry, uncovers new insights into middle and inner ear mechanics by simultaneously measuring structures and their vibrations in a cross-sectional plane over lateral ranges. However, it is vulnerable to a considerable increase in processing time because a significant amount of data are required to volumetrically reconstruct structural and vibrational information. A volumetric structural image requires three dimensions of data (x, y, k) where x and y are axes for lateral directions and k is the wavenumber. Whereas, three more dimensions of frequency (f), intensity (i), and duration time (t) for sound stimulus are added to the data in OCT vibrometry, representing a 6-D data set (x, y, k, t, f, i). Particularly, the time dimension (t) can be understood with an M-scan since the vibration of a sample is recorded at a fixed position for a stimulus duration. The required number of scans for one M-scan varies depending on the stimulus duration and the sweep rate of an adopted swept-laser. For example, if we use a 100 kHz swept-laser source to measure vibration for 10 ms with 10 combinations of sound stimuli consisting of 5 frequencies and 2 intensities, we will require 10,000 scans for one M-scan at each lateral position. This scales up the size of required data by ten thousand compared to acquiring structural information only. Not only the substantial increase in data size but also more processing steps contribute to the increase in processing time. This is because deriving vibrational amplitude and phase requires extracting, unwrapping and Fourier transforming interferometric phases. Therefore, it could take a lot of time to obtain data for reconstructing necessary information without careful planning for acquisition and processing.

This problem of increased processing time negatively affects biological and clinical applications of an OCT vibrometry system. Biological experiments require optimizing experimental conditions to obtain better results. However, the increased processing time can slow down both this

optimization process and acquisition of meaningful results, lowering experimental throughput. The lowered experimental throughput necessitates more samples and experimental time, reducing experimental efficiency. For clinical applications, this increased processing time can cause more discomfort of patients and delay the application of proper treatments by increasing diagnostic time. Hence, it is indispensable to reduce processing time for an OCT vibrometry system to be more appealing to biologists and clinicians.

To achieve this purpose, an architecture that acquire and process data efficiently for an OCT vibrometry system is proposed which exploits a commercial acquisition card and a GPU. Also, the proposed architecture is configured to accommodate any of the two different types of swept-lasers: linearly and non-linearly swept-lasers.

4.2 Method

4.2.1 Proposed architecture

Fig. 4.1 shows the proposed architecture that consists of an Alazartech card (ATS9373, Alazar Technologies Inc.), an NI digitizer (NI 5761, National Instruments) and an NI FPGA module (NI PXIe-7965R, National Instruments), Host, and NVIDIA GPU.
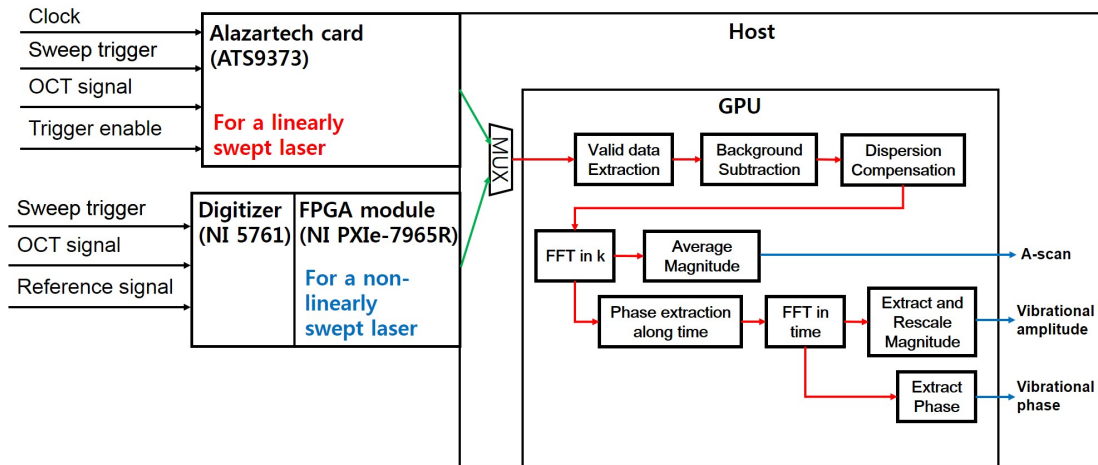
Figure 4.1: The proposed architecture for efficient acquisition and processing

An akinetic swept-laser (Insight Photonic Solutions Inc.) was adopted for a linearly swept-laser and the Alazartech card acquires a series of OCT signals from an OCT vibrometry system. For acquiring synchronously with the laser source, clock and sweep trigger signals from the laser source were connected to the Alazartech card. Also, the trigger enable signal, generated externally using the sweep trigger signal, was used to inform the Alazartech card of the starting point to acquire. For a non-linearly swept-laser, the NI digitizer and the NI FPGA module were used. A sweep trigger signal, OCT and reference signals were sampled by the NI digitizer and then the relative delay of the OCT signal to the sweep trigger signal was compensated. After the delay compensation, the OCT signal was calibrated to remove intra/inter sweep variabilities in the NI FPGA module by manipulating the reference signal as explained in Chapter 3. Once acquisition or calibration was done, the processed OCT signals were transferred to host memory, and the host transferred the received signals to the GPU for further processing. GPU hardware was chosen to reduce the time to process the transferred OCT signals, which can be achieved by processing each interferogram in a parallel way. The performance advantage is obtained by running the same piece of code concurrently on multiple data samples, exploiting the efficient GPU's SIMD (Single Instruction, Multiple Data) architecture

The software module to control the Alazartech card was coded with C while the NI FPGA module was implemented with LabView FPGA. Also, post-processing in the GPU was realized with CUDA C. Those modules were built as dynamic link library (DLL) with standard C external linkage, ready to be easily consumed within the Windows environment. A Python wrapper module was implemented to call the DLL functions from the Python program that is used to control the OCT vibrometry system.

4.2.2 Acquisition scheme

In order to acquire and transfer data to host efficiently, the Alazartech card is controlled as described in Fig. 4.2. This scheme is derived from the feature of the Alazatech card that it can acquire current data while transferring the previous one.

The Alazartech card starts to capture data right after detecting the rising edge of the trigger
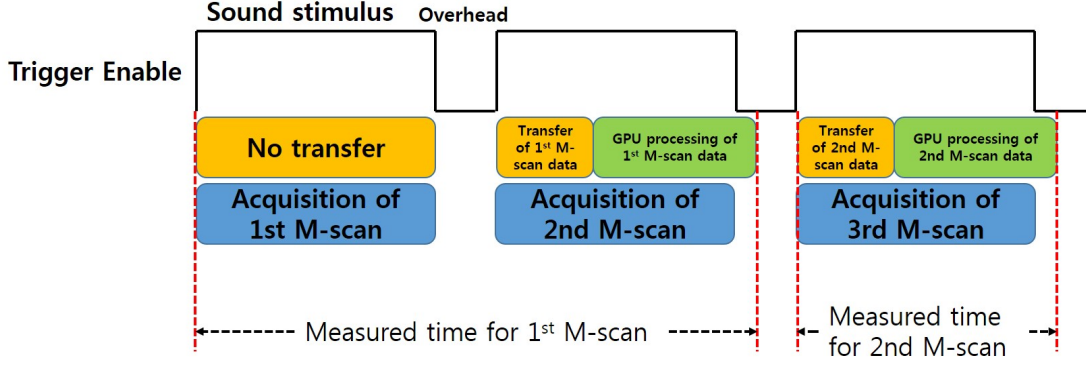
Figure 4.2: The acquisition scheme to efficiently acquire and transfer data

enable signal that consists of two time frames such as sound stimulus and overhead. The sound stimulus is the time when a sound is active to vibrate a sample while the overhead is an extra time before starting a new acquisition. At the first rising edge of the trigger enable signal, the first M-scan data are acquired. Since there is no previously acquired data, transfer does not occur. The Alazartech card starts to transfer the first M-scan data while acquiring the second M-scan data at the second rising edge of the trigger enable signal. The transferred data is then processed on GPU to derive vibrational amplitude and phase.

Using this scheme, the time to acquire and process M-scan data can be calculated as follows.

$$T_{Mscan}^{1} = T_{acq} + T_{over} + T_{trans} + T_{proc}$$

$$T_{Mscan}^{i} = T_{trans} + T_{proc}\ (i > 1) \tag{4.1}$$

$$T_{Mscan}^{total} = NT_{acq} + NT_{over} + T_{trans} + T_{proc}$$

where T_{acq}, T_{over}, T_{trans}, and T_{proc} are acquisition time (or stimulus time), overhead time, transfer time, and GPU processing time, respectively. T_{Mscan}^{i} and T_{Mscan}^{total} are measured time for acquiring and processing i-th M-scan data and total M-scan data respectively. N expresses the total number of M-scans.

Eq. (4.1) assumes the overhead time is determined such that T_{acq} + T_{over} is equal to or larger

34

than T$_{trans}$ + T$_{proc}$. That is, it should be defined as,

$$T_{over} \geq T_{trans} + T_{proc} - T_{acq} \qquad (4.2)$$

Defining the overhead time as shown in Eq. (4.2) guarantees avoidance of buffer overflow error in the Alarzartech card. This is because the speed of writing the memory in the Alazatech card is higher than that of reading since acquisition occurs more than transfer if the overhead is smaller than T$_{trans}$+T$_{proc}$-T$_{acq}$. Whereas, the overhead time satisfying this condition matches the speed of memory writing to that of memory reading, causing no buffer overflow error.

If we do not use this scheme, the overhead time should be selected such that

$$T_{over} \geq T_{trans} + T_{proc} \qquad (4.3)$$

As seen in Eq. (4.2) and Eq. (4.3), the proposed acquisition scheme reduces the overhead time by T$_{acq}$, allowing efficient time management.

In order to reduce T$_{over}$, it is important to decrease T$_{proc}$ because T$_{acq}$ and T$_{trans}$ are determined by stimulus time and the Alazartech card, respectively. This processing time reduction is achieved by implementing post-processing on GPU since it allows each interferogram in M-scan data to be processed simultaneously.

4.2.3 GPU processing

GPU was adopted to reduce processing time in order to determine T$_{over}$ in an efficient way as described in Eq. (4.2). In GPU processing, a set of transferred OCT signals from the Host to the GPU goes through the step of valid data extraction first which separates valid data points from invalid ones. This step is unique to the akinetic swept-laser, hence it is skipped when a non-linearly swept-laser is used. After the valid data extraction step, OCT signals are processed in the same way as the PhOCT technique does as explained in Chapter 2. The background signal is subtracted to remove background noise and dispersion, caused by difference in optics between reference and sample arms, is compensated. These dispersion compensated inteferograms are converted to

complex signals by FFT along the wavenumber dimension. From the complex signals, magnitudes are used to generate structural images, and phases are used to extract vibrational information. In order to induce vibrational amplitude and phase, the phases of the complex signals are extracted and unwrapped along time dimension, producing time domain phase signal. This time domain phase signal is FFTed and then the vibrational amplitude and phase are extracted at the frequency of interest.

4.3 Results and Discussion

The proposed architecture was tested in a host computer with an Intel Core i7-5930K (3.50 GHz) and NVIDIA Geforce GTX 980. And the akinetic swept-laser, with a 100 kHz sweep trigger rate, a 1310 nm center wavelength and a 100 nm bandwidth, was used. For a vibrating sample, a piezo electric element was adopted where a sinusoidal signal was applied to generate a periodic movement.

Before measuring the vibration of the piezo, T_{trans} and T_{proc} were measured iteratively to define appropriate T_{over} as Eq. (4.2) shows.

T_{acq} (ms)	T_{trans} (ms)	T_{proc} (ms)	$T_{trans} + T_{proc}$ (ms)	Duty cycle
10	3.351	5.930	9.281	Max
20	8.562	10.793	19.355	Max
30	13.945	15.359	29.304	Max
40	19.823	19.640	39.463	Max
50	22.552	26.909	49.461	Max

Table 4.1: Measured transfer and processing time in accordance with acquisition time.

Table 4.1 displays measured T_{trans} and T_{proc} resulting from averaging 100 measurements. Each measurement was made in the host computer against T_{acq} changing from 10 ms to 50 ms with a step of 10 ms. As T_{acq} increased, T_{trans} and T_{proc} also rose, keeping their sum within T_{acq}. Since T_{over} should be larger than or equal to zero, the minimum value of T_{over} is 0. In this table, duty cycle means the relative time duration of T_{acq} over $T_{acq} + T_{over}$ expressed as a percentage scale.

Because the duty cycle was defined to range from 1 to 99 in the host program, it was determined to be the maximum value of 99 since the minimum value of T_{over} is 0.

The proposed architecture in Fig. 4.1 was applied to acquire vibrational information at a certain depth, over a two-dimensional space (x and z), or over a three-dimensional space (x, y, and z). Those are called single point M-scan, BM-scan and volume M-scan, respectively. The term BM-scan originated from a B-scan of an M-scan since an M-scan is performed along x-axis similar to a B-scan which is an A-scan over that axis. Likewise, volume M-scan was named from a volume scan of an M-scan to express a three dimensional M-scan.

4.3.1 Single point M-scan

Single point M-scan is a method used to investigate vibrations at a specific position in depth. This method is useful to test a sample with multiple frequencies and multiple intensities of stimulus as shown in Fig. 4.3.

Single point M-scans require selecting a point in a B-scan image as indicated by the green arrow in Fig. 4.3(a), which was implemented in the host python program. At the selected point, a series of M-scans are performed in accordance with stimulus frequencies and expected sound pressure levels (SPL) which are determined by a user. In this experiment, the piezo was stimulated for 50 ms with 7 frequencies ranging from 4 kHz to 10 kHz with 1 kHz increment. Also, 12 intensities were used for each frequency, ranging from 60 dB SPL to 71 dB SPL with the step size of 1 dB SPL. This combination of frequencies and SPLs generated total 84 M-scans. For this experiment, it was assumed that 0.316 V generated the intensity of 60 dB SPL for the piezo, and the same voltages were applied along the frequency for simplicity. In reality, a speaker to be used is calibrated by measuring its intensity with a microphone, and the calibrated value is applied to generate a required SPL. The 84 M-scan data were processed to extract vibrational amplitude and phase as depicted in Fig. 4.3(b) and Fig. 4.3(c), respectively. The vibrational amplitudes are plotted in log scale in accordance with the stimulus frequencies since the applied voltage changes in dB scale.
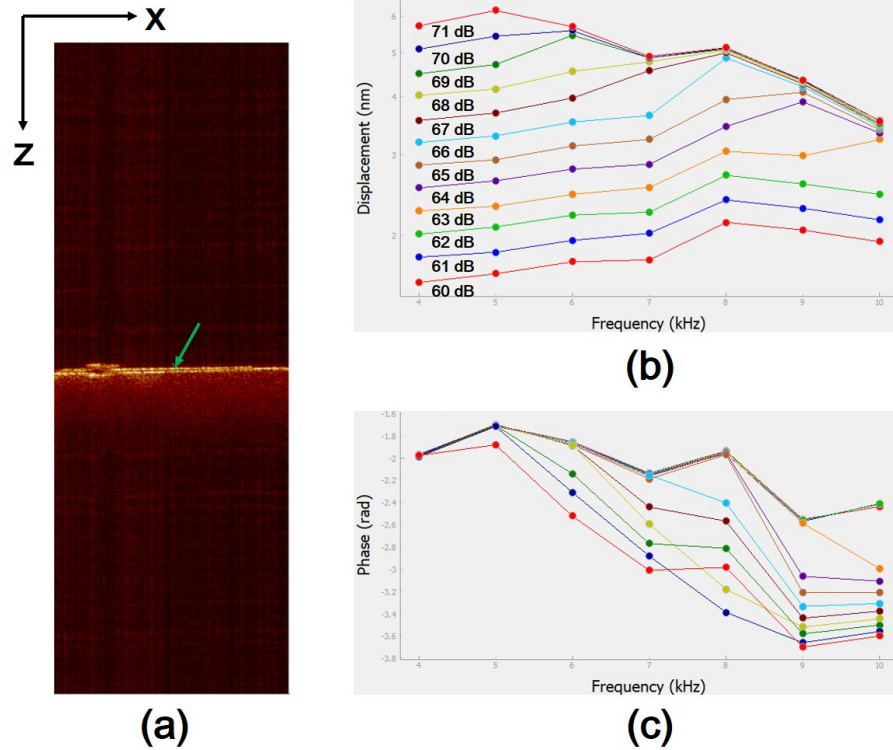
Figure 4.3: Single point M-scan results. (a) is a B-scan image to select a position for single point M-scan. The selected point is indicated by the green arrow. (b) and (c) are results of single point M-scan showing vibrational amplitude and phase, respectively along frequencies and intensities.

4.3.2 Two dimensional M-scan (BM-scan)

BM-scans provide information about cross-sectional vibration and structure. It requires a B-scan image, like the single point M-scan operation, in order to define two dimensional region of interest as shown in the green box in Fig. 4.4(a).

After selecting the region of interest, the piezo was stimulated by a 4 kHz sinusoidal signal with an intensity of 60 dB SPL. While stimulating, a series of M-scans were acquired and processed to generate a B-scan image, vibrational amplitudes and phases over the region. Fig. 4.4(b) shows the B-scan image while Fig. 4.4(c) and Fig. 4.4(d) are images of vibrational amplitude and phase, respectively overlaid on the B-scan image. The vibrational amplitudes and phases are colored to express their values which are around 1.6 nm and -113 degrees, respectively.
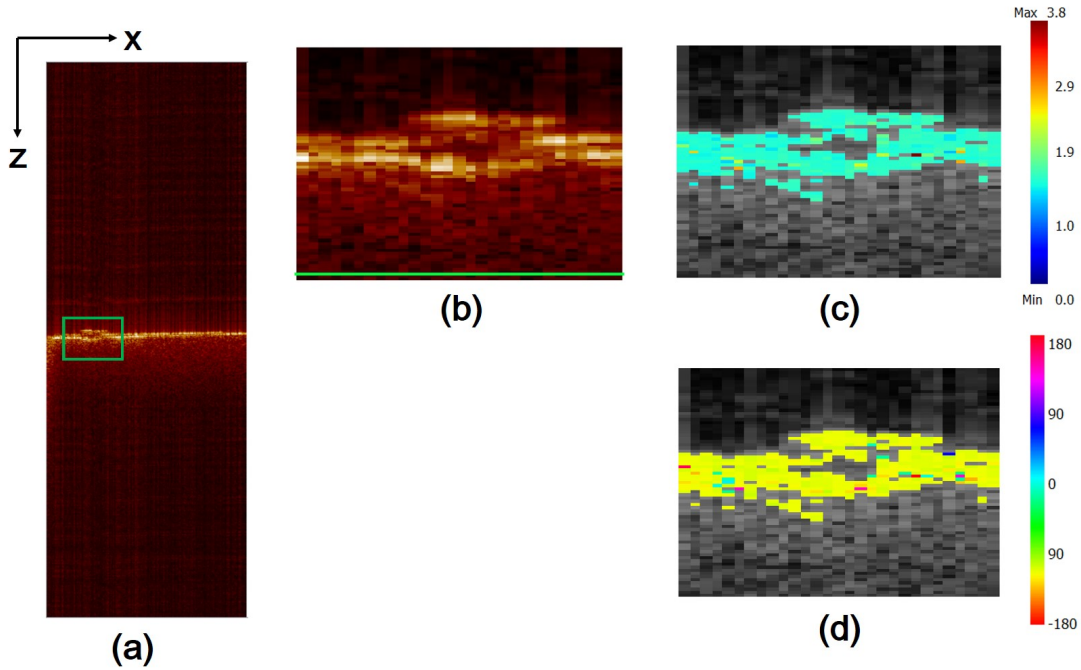
Figure 4.4: BM-scan results. (a) is a B-scan image to select a region of interest for BM-scan. The selected region is indicated by the green bax. (b), (c), and (d) are results from BM-scan. (b) is a B-scan image while (c) and (d) show vibrational amplitudes and phases, respectively overlaid on the B-scan image. The values are expressed in colors in (c) and (d).

4.3.3 Three dimensional M-scan (Volume M-scan)

It has been challenging to acquire and process a three dimensional M-scan due to the large data size as well as the processing burden. However, the proposed architecture enables three dimensional M-scans, or volume M-scans, by efficiently acquiring and processing the required data. Unlike the single point M-scan and BM-scan, a volume M-scan requires a volume image in order to define the volume region of interest on xy-plane.

A volume image is acquired by scanning a mirror over two orthogonal lateral ranges of (x, y), and is displayed in Fig. 4.5. Fig. 4.5(a) and Fig. 4.5(b) show one of B-scan images and a xy-plane image, respectively. The B-scan image is utilized not only to depict a cross-sectional profile, but also to determine z step and z range in Fig. 4.5(a) which define the starting and ending z indexes. Using those z indexes, xy-plane images are extracted and averaged along the z-axis to produce the
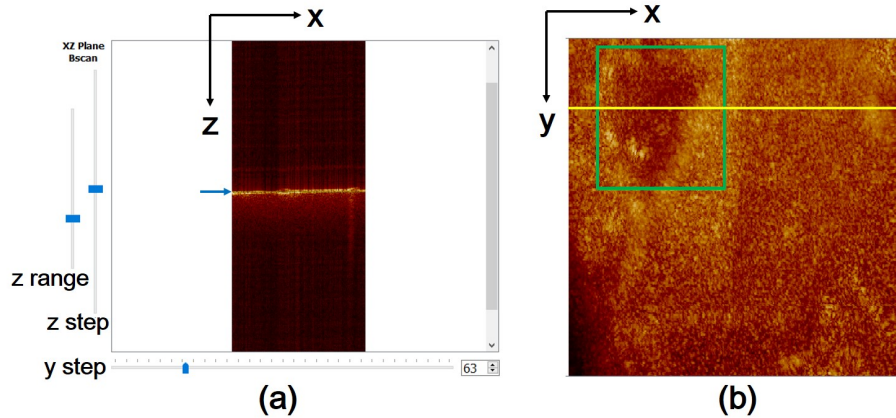
Figure 4.5: Selection of the volume region of interest for volume M-scan. (a) B-scan image defined on xz-plane. (b) xy-plane image. The blue arrow in (a) is used to indicate the selected depth to generate the xy-plane image. The green box in (b) is for defining the volume region of interest and the yellow horizontal line expresses the location on y-axis where the B-scan image is extracted.

xy-plane image in Fig. 4.5(b). The volume region of interest is selected on this xy-plane image. The yellow line in Fig. 4.5(b) moves in accordance with the y step bar in Fig. 4.5(a), showing a B-scan image at that location. After selecting the volume region, the piezo was stimulated with 4 kHz sinusoidal signal with the intensity of 70 dB SPL for 10 ms at each lateral position. The total lateral steps were 3,584: 56 steps for x-axis and 64 steps for y-axis, resulting in the total raw data size of 28.67 GB around three times higher than the Alazartech card memory (8 GB).

Fig. 4.6 displays the volume M-scan results on the selected volume region. Vibrational amplitudes and phases are mapped on the B-scan image as shown in Fig. 4.6(b) and Fig. 4.6(d), showing around 5 nm and -113 degrees, respectively. The xy-plane image in Fig. 4.6(c) was generated using the same method as that described for Fig. 4.6(b) and shows coincidence with the selected region. The B-scan image can be swept in accordance with y step bar to display corresponding structural and vibrational B-scan images.

4.4 Conclusion

We proposed a method to acquire and process M-scan data in an efficient way in order to reduce the time to obtain results. The proposed method utilized the feature of the Alazartech card that
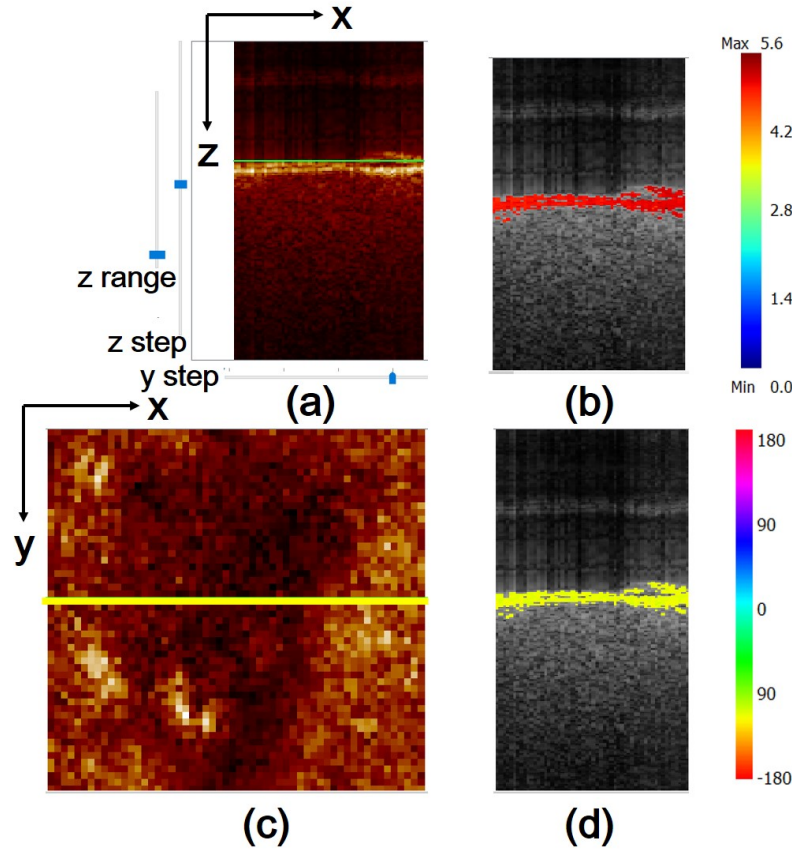
Figure 4.6: Volume M-scan results. (a) is a B-scan image while (b) and (d) display vibrational amplitudes and phases on the B-scan image, respectively. (c) is a xy-plane image generated using z range and z step in (a). The green horizontal line in (a) indicates selected z step while the yellow horizontal line in (c) indicates the location on y-axis where the B-scan image is extracted.

acquires data while transferring. This feature allows an efficient acquisition scheme by transferring and processing previous data while acquiring new data. Also, post-processing was implemented on GPU to reduce processing time. Both the acquisition scheme and the implementation on GPU enabled the sum of transfer and processing time to be within one acquisition, minimizing the overhead time necessary between acquisitions.

The proposed architecture was applied to perform a single point M-scan, BM-scan, and volume M-scan in order to obtain additional vibrational information at one axial point (z-axis), over two dimensions (x, z), and over three dimensions (x, y, z), respectively.

Therefore, not only does it improve experimental and diagnostic throughputs, but it also pro-

41

vides additional diagnostic information about the middle and inner ear by offering both structural and vibrational information. Moreover, the proposed method is not restricted to the field of OCT vibrometry and can be applicable to other fields that garner interferometric phases such as Doppler OCT and OCT elastography.

5. NOISE AND ARTIFACTS IN OPTICAL COHERENCE TOMOGRAPHY BASED VIBROMETRY

5.1 Introduction

There is growing interest in using Optical Coherence Tomography (OCT) for highly sensitive vibrational measurements in the auditory system. This is motivated by the ability to spatially resolve the vibratory response with subnanometer sensitivity. The detailed functional images generated have been used as a tool to probe fundamental auditory biomechanics and investigated as potential clinical diagnostics. These applications and more promise to drive the continued development of this nascent field.

A clear understanding of the fundamental noise statistics as well as inherent artifact due to adjacent reflectors is key to interpreting results and pushing the sensitivity limit of this technology for scientific and clinical applications. While various aspects have been investigated and reported in the literature there has not been a detailed and complete derivation with consistent notation and assumptions. The sensitivity for vibrometry is fundamentally linked to the noise statistics of the OCT signal, hence we start from the spectral interferogram and derive the noise statistics through the entire processing chain.

Before beginning we offer a brief review of the literatures surrounding this topic. Most of the work is not directly linked to OCT based vibrometry, but rather other related techniques that make use of the interferometric phase in OCT. The noise statistics for optical coherence tomography have been derived previously [12, 13, 14] to demonstrate the advantages of spectral interferometry over time-domain interferometry for OCT. These were derived for shot-noise, defining the fundamental limit to OCT sensitivity. Shortly thereafter, researchers began to develop techniques which exploited the phase-sensitivity inherent to spectral interferometry. In the context of spectral domain phase microscopy, Choma et al. [38] noted that the displacement sensitivity is proportional to $(2\text{SNR})^{-1/2}$, where SNR is the signal to noise ratio and we have corrected a factor of 2 multiplier.

Joo et al. [39] showed a similar result along with experimental verification of the distribution. Both results are for the time-domain phase. The noise statistics in the frequency domain were in part derived by Szkulmowski et al. [40] who noted the Rician distribution that arises for the magnitude of the phase for flow velocity estimation. Many of the relevant statistical arguments we will make have also been addressed in the context of Magnetic Resonance Imaging [41].

The artifacts induced by adjacent reflectors on interferometric phase measurements were addressed in the context of spectral domain phase microscopy by Ellerbee et al. [37]. They also provided compensating methods to avoid measurement distortion caused by an adjacent static object. More recently, Lin et al. [42] analytically and experimentally explored the phase retreival problem in OCT vibrometry. However, they did not handle the phase leakage problem in a general way in their derivation by only considering the case that the distance between neighboring and interesting reflectors is so small and an interferogram has a constant amplitude. Moreover, it is hard to see the effect of an error caused by an adjacent reflector only in both groups' derivation because they expressed equations to include both ideal and erroneous signals.

In this chapter the effect of additive noise on vibrometry was analyzed by considering the noise statistics through the entire processing chain with results for both the time-domain and frequency-domain phase. Likewise, we consider the artifact generated by adjacent reflectors, where overlapping sidebands lead to errors in magnitude, phase, and in some circumstances, the generation harmonics of the driving frequency. These are shown to be consistent with both numerical simulation and experiments with a swept-source OCT system.

5.2 Additive noise in OCT vibrometry

We will start by assuming all of the noise is additive since the main noise sources such as shot-noise, thermal noise, and relative intensity noise (RIN) are additive [43, 44, 45]. This is slightly more general, but consistent with prior derivations which assumed additive shot-noise. In order to determine the effect of additive noise on the extraction of the vibratory response, it is necessary to understand how the additive noise in the k-domain propagates through each mathematical operation, starting with the spectral interferogram H(k) and ending with the magnitude, $|v(z, f)|$, and

phase, $\angle v(z,f)$, of the vibratory response. A flow chart showing the processing steps along with the statistical results, e.g. the mean and standard deviation, is shown in Fig. 5.1. We define signal to noise ratio (SNR) for the OCT system in the conventional way, signal power divided by the second moment of the noise, i.e. $SNR = (s/n)^2$ or on a dB scale $SNR = 20log(s/n)$, where s is the signal energy and n is the second moment of the noise.
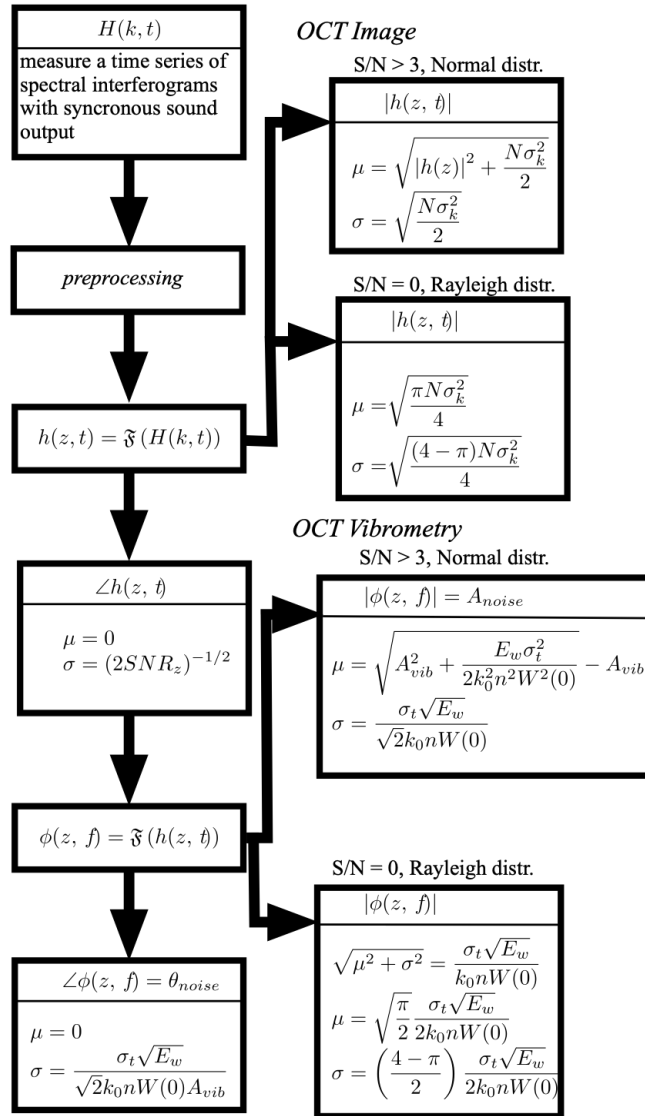
Figure 5.1: A flow chart showing the processing steps along with the statistical results such as distribution, mean and standard deviation.

A time series of spectral interferograms, H(k,t) is collected synchronously with sound output. We assume the DC term is subtracted from H(k,t) since H(k,t) is commonly preprocessed to remove it. Considering a single vibrating reflector and neglecting any autocorrelation,

$$H(k,t) = \frac{\rho}{b} S(k) \sqrt{R_R R_S} \, \cos(2kn\Delta z + 2k_0 n\delta z(t)) + n_k(k,t) \tag{5.1}$$

where k is the wavenumber, n is a refractive index, k_0 is the center wavenumber, ρ is the detector responsivity, S(k) is the power spectrum of the light source, R_R and R_S are the reflectivities of sample and reference arms of the interferometer, respectively, Δz is the pathlength difference between sample and reference arms, and δz(t) is the subresolution displacement of the reflector. The additive noise term, n_k(k,t), is independent, identically distributed (i.i.d) white Gaussian noise with zero mean and standard deviation of σ_k. It is also assumed that its statistical properties do not change over time, i.e. it is a stationary process.

The constant, b takes on the value 1 if both sides of the interferometer are collected and 2 if only one side is detected. In practice most swept-source based systems collect both sides using a balanced detector which has the added benefit of canceling the majority of the DC component and autocorrelation artifact. The remaining small DC component is typically subtracted in the preprocessing step noted above. Most spectrometer based systems only collect one side. In this case, the autocorrelation artifact remains and a large DC component must be subtracted in preprocessing.

Next we take the inverse Fourier transform of the interferometric signal, Eq. (5.1), to generate the complex signal, h(z,t), where z is the optical pathlength difference, related to the tissue depth (Δz) by z=2nΔz. The magnitude, $|h(z,t)|$, is the time series of A-scans or line images which are typically plotted against Δz. We would commonly take the mean along time and display the resulting line image $|h(z)|$ as the structural image.

The remaining processing steps are completed identically at each depth, hence for simplicity let us consider the interferometric signal at a single depth. Then, the L point discrete Fourier

transform (DFT) yields,

$$h(z = 2n\Delta z, t) = \frac{\rho s(0)\sqrt{R_R R_S}}{2b} e^{j2k_0 n\delta z(t)} + n_z(z = 2n\Delta z, t) \qquad (5.2)$$

where $s(0) = \sum_{i=1}^{N} S(k_i)$, N is total number of spectral channels, and n_z(z,t) is the complex noise in z-domain transformed from n_k(k,t). The noise statistics of the magnitude of Eq. (5.2) will follow a Rician distribution, as shown previously [40, 41]. The shape of the Rician distribution changes rapidly with the relative magnitude of signal over noise (S/N) where S and N are signal and noise magnitudes, respectively. When the S/N is greater than 3, the distribution is approximately Normal, leading to the mean and standard deviation of $|h(z,t)|$ shown in Fig. 5.1. This is the limit in which the OCT SNR is commonly derived, see for instance equation 7 in reference [13]. However when the signal is exactly zero, i.e. R_S is zero, the distribution n_z(z) has a Rayleigh distributed magnitude and a random phase with probability distribution that is uniform over 2π radians. The Rayleigh distribution arises because the real and imaginary components of n_z(z) are independent and normally distributed about 0 with a variance of $N\sigma_k^2/2$, [46]. For completeness the mean and standard deviation of $|h(z,t)|$ in the Rayleigh limit are also shown in Fig. 5.1. These results can be arrived at by simple variable substitution into Eq. (5.3) of reference [41], hence a detailed derivation is omitted.

Small scale vibrations (subresolution) of the reflector (δz) induce small changes in the phase of h(z) over time. The effect of the noise, n_z(z), on the phase of h(z), can be illustrated by complex domain analysis as shown in Fig. 5.2.

It can be seen from Fig. 5.2 that n_z(z) distorts the ideal phase with the phase noise, ϕ_{noise}(z), given by

$$\phi_{noise}(z) = \tan^{-1}\left(\frac{|n_z(z)|\sin(\phi_{n-i}(z))}{|h(z)| + |n_z(z)|\cos(\phi_{n-i}(z))}\right) \qquad (5.3)$$

In the limit that $|h(z,t)| >> |n_z(z,t)|$ Eq. (5.3) simplifies to
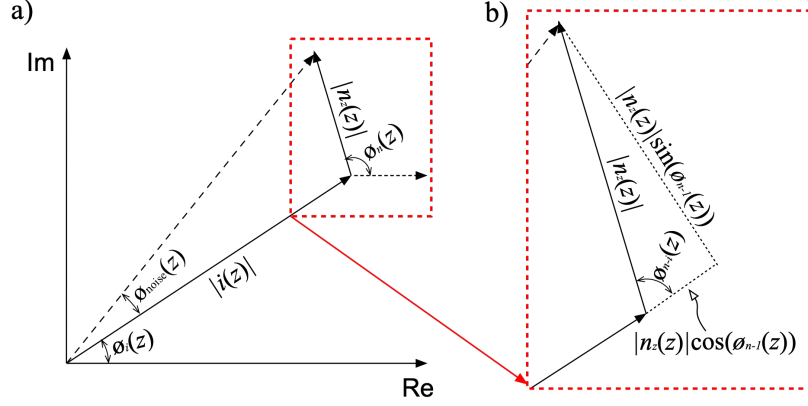
Figure 5.2: Graphical phase noise analysis in the complex domain. $|i(z)|$ and $\phi_i(z)$ are the magnitude and the phase of the ideal A-scan without noise. $|n_z(z)|$ and $\phi_n(z)$ are the magnitude and the phase of the noise, $|n_z(z)|$. $\phi_{n-i}(z)$ is the phase difference between the noise and ideal A-scan.

$$\phi_{noise}(z) \approx \frac{|n_z(z)|\sin(\phi_{n-i}(z))}{|h(z)|} \tag{5.4}$$

Assuming that the intensity of the reflector of interest does not change over time, the mean of the phase noise is

$$
\begin{aligned}
E[\phi_{noise}(z,t)] &\approx E\left[\frac{|n_z(z,t)|\sin(\phi_{n-i}(z,t))}{|h(z,t)|}\right] \\
&= \frac{E[|n_z(z,t)|(\sin(\phi_n(z,t))\cos(\phi_i(z,t)) + \cos(\phi_n(z,t))\sin(\phi_i(z,t)))]}{|h(z)|} \\
&= \frac{E[|n_z(z)|]E[\sin(\phi_n(z))]E[\cos(\phi_i(z,t))]}{|h(z)|} \\
&+ \frac{E[|n_z(z)|]E[\cos(\phi_n(z))]E[\sin(\phi_i(z,t))]}{|h(z)|} = 0
\end{aligned}
\tag{5.5}
$$

In Eq. (5.5), expected values of $|n_z(z,t)|$, $\cos(\phi_n(z,t))$, $\sin(\phi_n(z,t))$ and $\phi_i(z,t)$ are separated because they are independent of one another. Since n_z(z,t) and ϕ_n(z,t) are stationary in the statistical sense, the time dependence is dropped in calculating expectations of $|n_z(z,t)|$, $\cos(\phi_n(z,t))$, and $\sin(\phi_n(z,t))$. The noise phase is distributed uniformly over 2π [41], hence expected values of $\cos(\phi_n(z,t))$ and $\sin(\phi_n(z,t))$ are zero, leading to zero mean for the phase noise.

48

The standard deviation of the phase noise is expressed as

$$\sqrt{E[\phi_{noise}^2(z,t)]} \approx \sqrt{\frac{E[|n_z^2(z,t)|sin^2(\phi_{n-i}(z,t))]}{|h(z,t)|^2}}$$

$$= \sqrt{\frac{E[|n_z^2(z,t)|] - E[|n_z^2(z,t)|]E[\cos(2\phi_n(z,t) - 2\phi_i(z,t))]}{2|h(z,t)|^2}} \qquad (5.6)$$

$$= \sqrt{\frac{E[|n_z^2(z)|]}{2|h(z)|^2}} = \sqrt{\frac{N\sigma_k^2}{2|h(z)|^2}} = \frac{1}{\sqrt{2SNR_z}}$$

where $|h(z)|^2$ and $N\sigma_k^2$ are energies of the signal and noise in z-domain, respectively, and SNR_z is the signal to noise ratio in z-domain.

The uniformly distributed phase of the noise causes the cosine term to become zero, leaving the averaged noise energy in the numerator. The averaged noise energy is easily derived from the second moment of the Rayleigh distribution [41]. As seen in Eq. (5.5), the phase noise is expressed as the weighted sum of real and imaginary components of $n_z(z)$ which are stationary zero mean uncorrelated white Gaussian random processes. Therefore, the probability density function (PDF) of the phase noise is also stationary zero mean uncorrelated white Gaussian random process since it is the weighted sum of those processes [47], having a variance of $1/(2SNR_z)$. These results are in agreement with those of Joo et al. [39] derived in the context of spectral domain optical coherence phase microscopy.

The next step is to compute the Fourier transform of $\angle$h(z,t) along time to yield the magnitude and phase of the vibratory response as a function of depth and frequency. Again, since the same processing is done for each depth, we will explicitly consider the phase at only a single depth, (z_r) i.e. $\phi(z_r, t)$, without losing any generality. The time dependent phase at z_r is then

$$\phi(t) = 2k_0n\delta z(t) + n_t(t) = 2k_0nA_{vib}\cos(2\pi f_{vib}t + \theta_{vib}) + n_t(t) \qquad (5.7)$$

where t is the time index, A_{vib}, f_{vib}, and θ_{vib} are vibrational amplitude, frequency, and phase, respectively, n_t(t) is the time domain phase noise, and we have dropped the z_r to simplify notation.

The time domain phase in Eq. (5.7) is described with a sinusoidal function to express an ideal

vibration [48]. Generally, any sound can be represented by a sum of sinusoidal waves, hence this does not significantly limit the applicability of the derivation. As shown above, $n_t(t)$ is a stationary white Gaussian noise that has a zero mean and standard deviation of the square root of $1/2SNR_z$.

The next step is to take the Fourier transform of $\phi(t)$ to yield the complex vibratory response, $\phi(f)$ at z_r. Assuming M samples in the time series, the frequency domain vibrational signal is expressed as

$$\phi(f) = 2k_0 n \delta z(f) + n_f(f) = M k_0 n A_{vib} \delta(f \pm f_{vib}) e^{\mp j\theta_{vib}} + n_f(f) \tag{5.8}$$

where $n_f(f)$ is the frequency domain phase noise transformed from $n_t(t)$. The real and imaginary components of $n_f(f)$ are also stationary zero mean uncorrelated white Gaussian since they are simply a weighted sum of $n_t(t)$. Their variances are $M\sigma_t^2/2$ [46] where σ_t^2 is the variance of $n_t(t)$.

At the frequency of the stimulus (f_{vib}) the vibrational amplitude (A_{vib}) and phase (θ_{vib}) are given by

$$\begin{aligned}
\frac{\phi(f_vib)}{Mk_0 n} &= A_{vib} e^{j\theta_{vib}} + \frac{n_f(f_{vib})}{Mk_0 n} \\
&= \left(A_{vib} \cos(\theta_{vib}) + \frac{n_{f-real}(f_{vib})}{Mk_0 n} \right) + j \left(A_{vib} \sin(\theta_{vib}) + \frac{n_{f-imag}(f_{vib})}{Mk_0 n} \right)
\end{aligned} \tag{5.9}$$

where we have scaled the phase by the factor $Mk_0 n$ to convert to nanometers from radians, $n_{f-real}(f)$ and $n_{f-imag}(f)$ are the real and imaginary component of $n_f(f)$.

The measured vibrational amplitude, A_{mea}, is the magnitude of Eq. (5.9). As can be seen in Eq. (5.9), the measured amplitude differs from true amplitude, A_{vib}, due to noise, i.e.

$$A_{noise} = A_{mea} - A_{vib} \tag{5.10}$$

where A_{noise} is the amplitude detection noise.

The statistical properties of A_{noise} depends on the magnitude of A_{vib}. When A_{vib} is equal to 0, A_{mea} is Rayleigh distributed [41], hence A_{noise} follows the Rayleigh distribution. The sensitivity of an OCT vibrometry system is typically defined in this limit by observing the noise of a frequency

band where there is no vibration. In this case, the square root of the second moment of A_{noise}, i.e. $\sqrt{\mu^2 + \sigma^2}$, is

$$\sqrt{E[A_{noise}^2]} = \frac{\sigma_t}{k_0 n \sqrt{M}} \tag{5.11}$$

Eq. (5.11) shows the root mean square (RMS) value of A_{noise} and can be used to predict the performance of vibratory measurements given SNR in z-domain. The real and imaginary components of A_{noise} are independent and normally distributed with zero mean and the standard deviation of $\sigma_t / k_0 n \sqrt{2M}$ when $A_{vib} = 0$.

When $A_{vib} \neq 0$, the noise is Rician distributed, however it can be approximated as a Gaussian distribution in the limit that the signal is larger than the standard deviation of the noise. It has been shown previously that a $s/n > 3$ (i.e. $A_{vib} \geq 3\sigma_t / k_0 n \sqrt{2M}$) was sufficient to allow this approximation [41]. In OCT vibrometry, a measured displacement signal is typically in the range of few to one hundred nanometers [1, 2, 6, 49] while noise standard deviations are commonly less than one nanometer [2, 49]. Practically, the majority of measurements will have s/n that satisfy this criteria. Thus, the distribution of the detected magnitude in OCT vibrometry can be considered to be Gaussian whose mean and standard deviation are the square root of $A_{vib}^2 + \sigma_t^2 / 2M k_0^2 n^2$ and $\sigma_t^2 / 2M k_0^2 n^2$, respectively [41], leading A_{noise} to the results in Eq. (5.12).

$$\begin{aligned} E[A_{noise}] = E[A_{mea} - A_{vib}] = E[A_{mea}] - A_{vib} = \sqrt{A_{vib}^2 + \frac{\sigma_t^2}{2M k_0^2 n^2}} - A_{vib} \\ \sqrt{E[(A_{noise} - E[A_{noise}])^2]} = \sqrt{E[(A_{mea} - \mu_{mea})^2]} = \frac{\sigma_t}{k_0 n \sqrt{2M}} \end{aligned} \tag{5.12}$$

where μ_{mea} is the mean of A_{mea}.

The noise in extracting the phase of the vibration, θ_{vib}, in the frequency domain is derived using Eq. (5.5) and Eq. (5.6) since the time domain phase noise is additive zero mean white Gaussian,

yielding

$$E[\theta_{noise}] = 0$$

$$\sqrt{E[\theta_{noise}^2]} = \frac{1}{\sqrt{2SNR_f}} = \sqrt{\frac{M\sigma_t^2}{2(Mk_0nA_{vib})^2}} = \frac{\sigma_t}{A_{vib}k_0n\sqrt{2M}}$$

(5.13)

where θ_{noise} is the phase detection noise. The phase detection noise is also Gaussian distributed, and its standard deviation is the same as that of A_{noise}, Eq. (5.12), except for the A_{vib} term in the denominator.

5.3   Artifacts due to adjacent reflectors, phase leakage

It is well known that adjacent reflectors can influence the measured interferometric phase at their respective peaks [37]. Since the vibrational amplitude and phase are derived from the interferometric phase, the interaction of adjacent reflectors can introduce systematic errors that are not accounted for in the statistical noise arguments made above. In order to investigate these artifacts theoretically we start by restating Eq. (5.1) for two adjacent reflectors, i.e

$$H(k,t) = \frac{\rho}{b}S(k)\left[\sqrt{R_R R_{S1}}\cos(2kn_1\Delta z_1 + 2k_0n_1\delta z_1)) + \sqrt{R_R R_{S2}}\cos(2kn_2\Delta z_2 + 2k_0n_2\delta z_2))\right]$$

(5.14)

where R_{S1}, n_1, Δz_1, and δz_1 are the reflectivity, the refractive index, the pathlength difference, and the displacement of a reflector of interest while R_{S2}, n_2, Δz_2, and δz_2 are of an adjacent reflector.

Considering L point DFT, the complex signal h(z) at a single depth can be expressed in the same way as Eq. (5.2), yielding

$$
\begin{aligned}
h(z = 2n_1\Delta z_1) = & \frac{\rho s(0)\sqrt{R_R R_{S1}}}{2b}e^{j2k_0n_1\delta z_1} + \\
& \frac{\rho|s(2n_1\Delta z_1 - 2n_2\Delta z_2)|\sqrt{R_R R_{S2}}}{2b}e^{\angle s(2n_1\Delta z_1 - 2n_2\Delta z_2) + j2k_0n_2\delta z_2}
\end{aligned}
$$

(5.15)

where $|s(z)|$ and $\angle s(z)$ are the magnitude and the phase of s(z), and $\angle s(0)$ is removed because s(0) is the DC component of s(z) which has only real component.

The vibrational signal from the reflector of interest is extracted by detecting the phase of h(z=$2n_1\Delta z_1$). However, as Eq. (5.15) suggests, extracting the phase is affected by the additional term originated from the adjacent reflector. In order to analyze the effect of the adjacent reflector, the phase error is derived in the same way as shown in Fig. 5.2 to yield

$$
\begin{aligned}
\phi(2n_1\Delta z_1) &= \tan^{-1}\left(\frac{\sqrt{\frac{R_{S2}}{R_{S1}}}|s(\Delta z_{1-2})|\sin(\angle s(\Delta z_{1-2}) + 2k_0(n_2\delta z_2 - n_1\delta z_1))}{|s(0)| + \sqrt{\frac{R_{S2}}{R_{S1}}}|s(\Delta z_{1-2})|\cos(\angle s(\Delta z_{1-2}) + 2k_0(n_2\delta z_2 - n_1\delta z_1))}\right) \\
&\approx \tan^{-1}\left(\frac{|s(\Delta z_{1-2})|\sin(\angle s(\Delta z_{1-2}) + 2k_0 n(\delta z_2 - \delta z_1))}{|s(0)| + |s(\Delta z_{1-2})|\cos(\angle s(\Delta z_{1-2}) + 2k_0 n(\delta z_2 - \delta z_1))}\right) \\
&\approx \frac{|s(\Delta z_{1-2})|}{|s(0)|}\sin(\angle s(\Delta z_{1-2}) + 2k_0 n(\delta z_2 - \delta z_1))
\end{aligned}
$$

(5.16)

where Δz_{1-2} is $2n_1\Delta z_1 - 2n_2\Delta z_2$, the relative pathlength difference between the adjacent reflectors.

In Eq. (5.16), the initial term is approximated by assuming that $R_{S1} \approx R_{S2}$, $n_{S1} \approx n_{S2}$ because those values are similar in the same tissue, and that $|s(0)| >> |s(\Delta z_{1-2})|$ for simple expression. The angle of s(Δz_{1-2}) included in the sine function is constant with respect to time as long as the spectral shape of a source does not change during the measurement. Within a vibrating tissue, reflectors of interest and their nearest neighbors exhibit similar vibrational amplitude and phase [42, 2], meaning that $\delta z_1 \approx \delta z_2$. In this case, Eq. (5.16) approaches the following form.

$$
\phi_{error}(t) = \frac{|s(\Delta z_{1-2})|}{|s(0)|}\sin(\angle s(\Delta z_{1-2}))
$$

(5.17)

where the time index of t is added to express the phase error along time, $|s(0)|$ is the magnitude of an interesting reflector while $|s(\Delta z_{1-2})|$ and $\angle s(\Delta z_{1-2})$ are the magnitude and the phase of an adjacent reflector at the position of the interesting one. Eq. (5.17) shows that the phase error is expressed as constant with respect to time, changing the DC level of a vibrational signal in the time domain. This constant phase error centers at 0 Hz in the frequency domain, being separated from a vibrational signal in that domain. This separation makes the extraction of vibrational magnitude

and phase not affected.

Another important case is when $\delta z_1(t)$ and $\delta z_2(t)$ are not similar as seen in [37]. In this case, the vibrational amplitude of the combined vibrational signal, $\delta z_2(t) - \delta z_1(t)$, is large, where Eq. (5.16) needs to be further derived with the assumption that $\delta z_2(t) - \delta z_1(t) = A_{cvib}\cos(2\pi f_{vib}t + \theta_{cvib})$. This assumption is appropriate because a vibrating tissue oscillates with the same frequency as stimulus [2, 42].

$$
\begin{aligned}
\phi_{error}(t) &= \frac{|s(\Delta z_{1-2})|}{|s(0)|}\sin(\angle s(\Delta z_{1-2}) + 2k_0 n(\delta z_2(t) - \delta z_1(t))) \\
&= \frac{|s(\Delta z_{1-2})|}{|s(0)|}\sin(\angle s(\Delta z_{1-2}) + 2k_0 n A_{cvib}\cos(2\pi f_{vib}t + \theta_{cvib})) \\
&= \frac{|s(\Delta z_{1-2})|}{|s(0)|}\sin(\angle s(\Delta z_{1-2}))\cos(2k_0 n A_{cvib}\cos(2\pi f_{vib}t + \theta_{cvib})) \\
&\quad + \frac{|s(\Delta z_{1-2})|}{|s(0)|}\cos(\angle s(\Delta z_{1-2}))\sin(2k_0 n A_{cvib}\cos(2\pi f_{vib}t + \theta_{cvib})) \\
&= \frac{|s(\Delta z_{1-2})|}{|s(0)|}\sin(\angle s(\Delta z_{1-2})) \\
&\quad \times \left[J_0(2k_0 n A_{cvib}\cos(\theta_{cvib})) + \sum_{m=2l}^{\infty} 2J_m(2k_0 n A_{cvib}\cos(\theta_{cvib}))(-1)^l\cos(2\pi m f_{vib}t)\right] \\
&\quad \times \left[J_0(2k_0 n A_{cvib}\sin(\theta_{cvib})) + \sum_{m=2l}^{\infty} 2J_m(2k_0 n A_{cvib}\sin(\theta_{cvib}))\cos(2\pi m f_{vib}t)\right] \\
&\quad + \frac{|s(\Delta z_{1-2})|}{|s(0)|}\sin(\angle s(\Delta z_{1-2})) \left[\sum_{m=2l-1}^{\infty} 2J_m(2k_0 n A_{cvib}\cos(\theta_{cvib}))(-1)^{l+1}\sin(2\pi m f_{vib}t)\right] \\
&\quad \times \left[\sum_{m=2l-1}^{\infty} 2J_m(2k_0 n A_{cvib}\sin(\theta_{cvib}))cos(2\pi m f_{vib}t)\right] \\
&\quad + \frac{|s(\Delta z_{1-2})|}{|s(0)|}\cos(\angle s(\Delta z_{1-2})) \left[\sum_{m=2l-1}^{\infty} 2J_m(2k_0 n A_{cvib}\cos(\theta_{cvib}))(-1)^{l+1}\cos(2\pi m f_{vib}t)\right] \\
&\quad \times \left[J_0(2k_0 n A_{cvib}\sin(\theta_{cvib})) \sum_{m=2l}^{\infty} 2J_m(2k_0 n A_{cvib}\sin(\theta_{cvib}))cos(2\pi m f_{vib}t)\right] \\
&\quad - \frac{|s(\Delta z_{1-2})|}{|s(0)|}\cos(\angle s(\Delta z_{1-2}))
\end{aligned}
$$

$$\times \left[J_0(2k_0nA_{cvib}\cos(\theta_{cvib})) + \sum_{m=2l}^{\infty} 2J_m(2k_0nA_{cvib}\cos(\theta_{cvib}))(-1)^l \cos(2\pi mf_{vib}t) \right]$$

$$\times \left[\sum_{m=2l}^{\infty} 2J_m(2k_0nA_{cvib}\sin(\theta_{cvib}))\sin(2\pi mf_{vib}t) \right] \tag{5.18}$$

where A_{cvib} and θ_{cvib} are the combined vibrational amplitude and phase, respectively and $J_m(x)$ is the Bessel function of the first kind.

To express Eq. (5.18) in a more simple way, θ_{cvib} is assumed to be zero, yielding

$$\phi_{error}(t) = \frac{|s(\Delta z_{1-2})|}{|s(0)|}\sin(\angle s(\Delta z_{1-2})) \left[J_0(2k_0nA_{cvib}) + \sum_{m=2l}^{\infty} 2J_m(2k_0nA_{cvib})(-1)^l \cos(2\pi mf_{vib}t) \right]$$

$$+ \frac{|s(\Delta z_{1-2})|}{|s(0)|}\cos(\angle s(\Delta z_{1-2})) \sum_{m=2l-1}^{\infty} 2J_m(2k_0nA_{cvib})(-1)^{l+1}\sin(2\pi mf_{vib}t), \; l = 1,2,3,\cdots \tag{5.19}$$

As seen in Eq. (5.19), harmonic components of the vibrational signal will be generated by an adjacent reflector. However, in the limit that A_{cvib} is small, $J_0(2k_0nA_{cvib})$ approaches 1 and the infinite sums over higher orders approach zero, hence Eq. (5.19) simplifies to Eq. (5.17). This analysis is in agreement with findings from [42] that the larger differential displacement shows more harmonic signals while the small one rarely displays them. When the adjacent reflector is a static object, $\delta z_2(t)$ becomes constant and is grouped to $\angle s(\delta z_{1-2})$ in Eq. (5.16). In this case, harmonic components of the phase error depend only on $\delta z_1(t)$ since it solely determines A_{cvib} and θ_{cvib} of the combined vibrational signal. This means that harmonic components become dominant as the vibrational amplitude of an interesting reflector increases while they become attenuated as it decreases.

The fundamental frequency component (k=1) in Eq. (5.18) has the greatest impact on the measured vibrational amplitude and phase at the stimulus frequency. If we truncate the infinite series

of Eq. (5.18) after k=1, then we can simply Eq. (5.18) to

$$
\begin{aligned}
\phi_{error}(t) &\approx G_{err} J_0(2k_0 n A_{cvib} \sin(\theta_{cvib})) 2J_1(2k_0 n A_{cvib} \cos(\theta_{cvib})) \cos(2\pi f_{vib} t) \\
&- G_{err} J_0(2k_0 n A_{cvib} \cos(\theta_{cvib})) 2J_1(2k_0 n A_{cvib} \sin(\theta_{cvib})) \sin(2\pi f_{vib} t) \\
&\approx 2k_0 n G_{err} A_{cvib} [\cos(\theta_{cvib}) \cos(2\pi f_{vib} t) - \sin(\theta_{cvib}) \sin(2\pi f_{vib} t)] \\
&= 2k_0 n G_{err} A_{cvib} \cos(2\pi f_{vib} t + \theta_{cvib}), /G_{err} = \frac{|s(\Delta z_{1-2})| \cos(\angle s(\Delta z_{1-2}))}{|s(0)|}
\end{aligned}
\tag{5.20}
$$

where θ_{cvib} is the combined phase of $\delta z_2(t) - \delta z_1(t)$, and G_{err} is the gain of the phase error applied to the combined vibrational signal.

In Eq. (5.20), the time domain phase error is simplified to the fundamental component, and then is further approximated using the characteristic of the Bessel function of the first kind that $J_0(x) \approx 1$ and $2J_1(x) \approx x$ when x is small. Analyzing the effect of the phase error in Eq. (5.20) in the frequency domain using Fig. 5.2, the vibrational amplitude error is

$$
A_{error} = \sqrt{A_{vib}^2 + (G_{err} A_{cvib})^2 + 2G_{err} A_{cvib} A_{vib} \cos(\theta_{cvib} - \theta_{vib})} - A_{vib}
\tag{5.21}
$$

In the same way, the error that occurs when extracting the vibrational phase in the frequency domain is calculated as

$$
\theta_{error} = \tan^{-1}\left(\frac{G_{err} A_{cvib} \sin(\theta_{cvib} - \theta_{vib})}{A_{vib} + G_{err} A_{cvib} \cos(\theta_{cvib} - \theta_{vib})} \right)
\tag{5.22}
$$

Assuming $A_{vib} >> G_{err} A_{cvib}$, minimum and maximum values for the magnitude of each error are determined as

$$
\begin{aligned}
0 &\leq |A_{error}| \leq G_{err} A_{cvib} \\
0 &\leq |\theta_{error}| \leq \tan^{-1}\left(\frac{G_{err} A_{cvib}}{A_{vib}} \right)
\end{aligned}
\tag{5.23}
$$

In Eq. (5.23), the maximum amplitude detection error is achieved when $\theta_{cvib} = \theta_{vib}$ or $\theta_{cvib} = \theta_{vib} \pm \pi$ while the minimum one is when $A_{cvib} = 0$ or $\theta_{cvib} = \cos_{-1}(-G_{err} A_{cvib}/2A_{vib}) + \theta_{vib}$

where $G_{err}A_{cvib}/2A_{vib} \leq 1$. Also, the minimum phase detection error is calculated by making the numerator term zero whereas the maximum one is achieved when θ_{cvib} is perpendicular to θ_{vib}. It is seen from Eq. (5.23) that both G_{err} and A_{cvib} affect amplitude and phase detection errors, and the relative magnitude of A_{vib} over A_{cvib} plays important role in determining the phase detection error. Since A_{vib} and A_{cvib} are not controllable, a convenient method to reduce both detection errors is to increase the relative magnitude of the reflector of interest over the adjacent one, which is usually done by careful selection of window function.

5.4 Results

5.4.1 Simulation Results

Next we decided to numerically simulate an M-scan of a vibrating reflector. This allowed us, in a very controlled setting where we know for certain that all of the noise is additive, to verify that the equations we have derived hold. The simulation was executed in MATLAB (Mathworks, Inc). The set of inteferograms were modeled using Eq. (5.1) such that $\rho S(k)\sqrt{R_R R_S}/b = 1$, $\Delta_z = 1.713$ mm, $k_0 = 2\pi/1310$ nm, n = 1. The wavelength bandwidth and the total number of spectral channels (N) were set to be 100 nm and 2000, respectively. The vibrational signal $\delta z(t)$ was modeled using Eq. (5.7) to have that $A_{vib} = 10$ nm, $\theta_{vib} = 30$ degree. And the vibrational frequency f_{vib} was defined to be the digital frequency of 0.1 which means $f_{vib} = 0.1 \times$A-scan rate. The number of points for the vibrational signal (M) was set to be 1000 points. This vibrational signal was embedded into the modeled interferograms to make one set of M-scan data as shown in Eq. (5.1). The k-domain noise $n_k(k,t)$ in Eq. (5.1) was shaped to be additive Gaussian which has zero mean and standard deviation (σ_k) ranging from 0 to 0.1, and to be stationary so that each interferogram has the same statistical properties. The change in the standard deviation (σ_k) was intended to see the effects of additive noise on vibratory measurements.

Fig. 5.3(a) shows one of the modeled interferograms, $H(k,t)$, in the time-series with a k-domain noise standard deviation of 0.1. Fig. 5.3(b) displays the magnitude response of the fast Fourier transform of that signal, $|h(z,t)|$, where a reflector is located at index 200 and has a s/n of
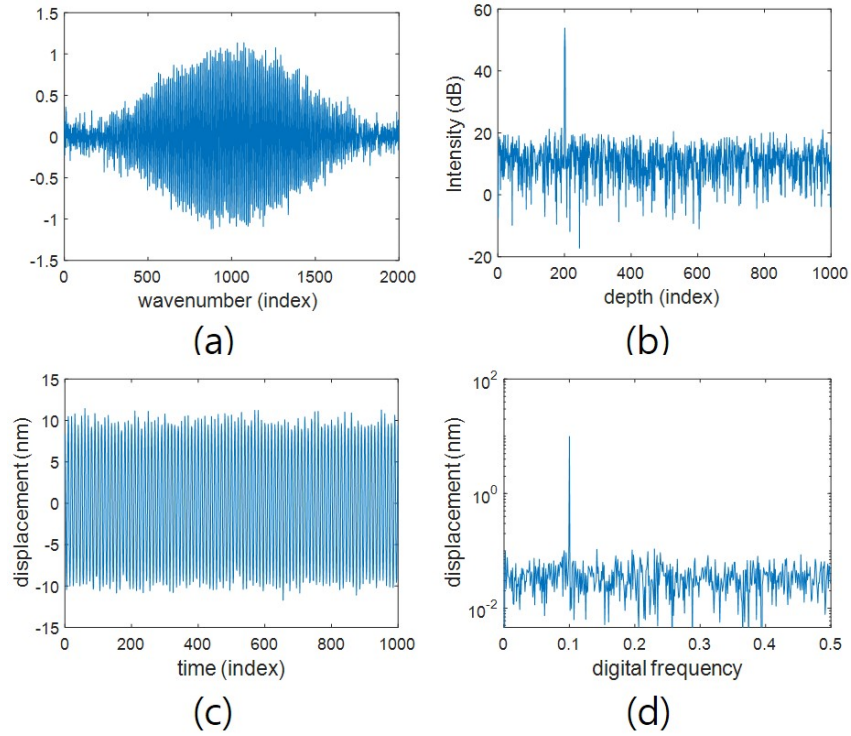
Figure 5.3: (a) One of modeled interferograms with additive noise. (b) A-scan of (a). (c) Time domain vibrational signal extracted from a set of A-scans. (d) Frequency domain vibrational signal transformed from (c).

40.97 dB calculated from 20log10(s/n). From the complex signal the time-domain phase, $\phi(200, t)$, can be extracted at the location of the reflector to yield the trace in Fig. 5.3(c). At this stage the sinusoidal vibration of the reflector is apparent. A fast Fourier transform yields the magnitude response of the vibration $|\phi(200, f)|$ shown in Fig. 5.3(d), and vibrational amplitude and phase are extracted at the normalized digital frequency of 0.1, $|\phi(200, f = 0.1)|$, showing 9.99 nm and 29.86°, respectively. Note, the displacement in Fig. 5.3(d) was placed on a log-scale in order to make the noise more visible. The k-domain noise was generated with the MATLAB function of $randn$ multiplied by the desired standard deviation to generate Gaussian distributed random numbers with zero mean. For one M-scan data set, the noise was generated 1000 times with the same mean and standard deviation to be added to each modeled interferogram as seen in Eq. (5.1). These M-scan data were iteratively acquired to calculate statistical properties of experimental amplitude

and phase detection noises. Then the theoretical mean and standard deviation of the amplitude, $|\phi(z, f)|$, were calculated for comparison to simulation results.

Figure 5.4: Comparison of statistical properties of amplitude detection noise. (a) and (b) are acquired from 300 measurements while (c) and (d) from 3000 measurements. (a), (c) and (b), (d) show comparison of amplitude detection noise mean and standard deviation, respectively. Red line means the result from Eq. (5.12) whereas blue one means from experimentally acquired detection noise.

The mean and standard deviation of the amplitude detection noise (A_{noise}), the measured vibrational amplitude at $\phi(200, f = 0.1)$ subtracted by the true vibrational amplitude A_{vib}, were calculated from the modeled interferograms and plotted in Fig. 5.4 as a function of k-domain noise standard deviation, σ_k. The bottom x-axis on each plot is σ_k with the corresponding SNR plotted

on the top x-axis. Note that the SNR is always well above 9.5 dB (s/n=3), so we are in the normal distribution limit. The y-axis is the noise mean in Fig. 5.4(a,c) and noise STD in Fig. 5.4(b,d). The top and bottom rows in the figure differ by the number of M-scans used to generate the statistics, 300 top and 3000 bottom. A qualitative comparison of the top and bottom rows shows the expected trend: as we increase the number of samples used to generate the statistic, the results of the simulation more closely match the theory. The noise mean oscillates above and below the theoretical values. The standard deviation likewise oscillates above and below the theoretical line and clearly follows the same trend. Also, it is shown that mean and standard deviation of amplitude detection noise increases as expected with an increase in the k-domain noise standard deviation. This is due to increase in the standard deviation (σ_t) of the time domain phase noise $n_t(t)$ in Eq. (5.7) caused by decrease in SNR in z-domain. However, the degree of the increase differs from each other: the amplitude detection noise standard deviation is high while the amplitude detection noise mean is low. This is because time domain noise has less effect on the calculation of mean because the true vibrational amplitude (A_{vib}) is dominant in the square root operation while it has more on standard deviation since the noise directly affects the standard deviation, as shown in Eq. (5.12).

The phase detection noise (θ_{noise}) was calculated by subtracting the true vibrational phase (θ_{vib}) from the measured one ($\theta_{mea} = \angle\phi(200, f = 0.1)$), and its mean and standard deviation was plotted in Fig. 5.5 in accordance with $sigma_k$. As seen in the results of A_{noise} in Fig. 5.4, the mean and standard deviation of θ_{noise} match the theory more closely as the number of used samples increases. Both mean and standard deviation shows the same trend while fluctuating slightly about the theory. Also, the standard deviation of the phase detection noise grows more rapidly in accordance with the k-domain noise standard deviation compared to the mean. This shows the same trend as the amplitude detection noise because time domain phase noise directly affects the standard deviation while it has no effect on the mean as seen in Eq. (5.13). As seen in the amplitude detection noise plots, the increase in the standard deviation of θ_{noise} results from the decrease in SNR since this brings about rise up of σ_t. Therefore, these MATLAB simulation results give us confidence that the derived equations are correct within the assumptions of additive
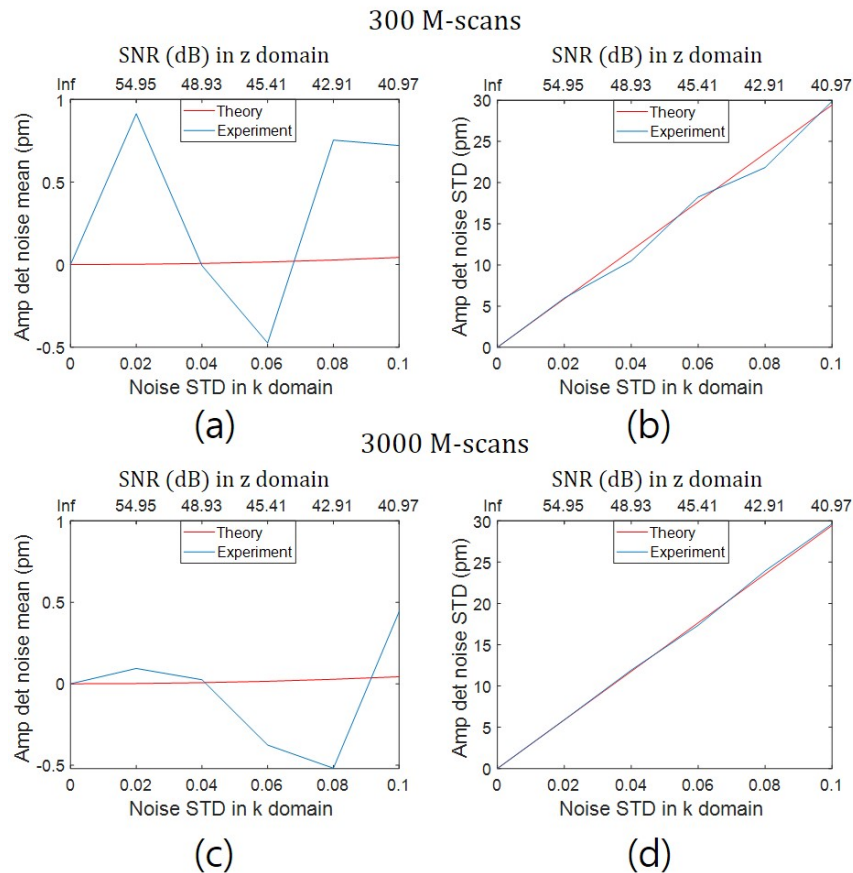
300 M-scans

3000 M-scans
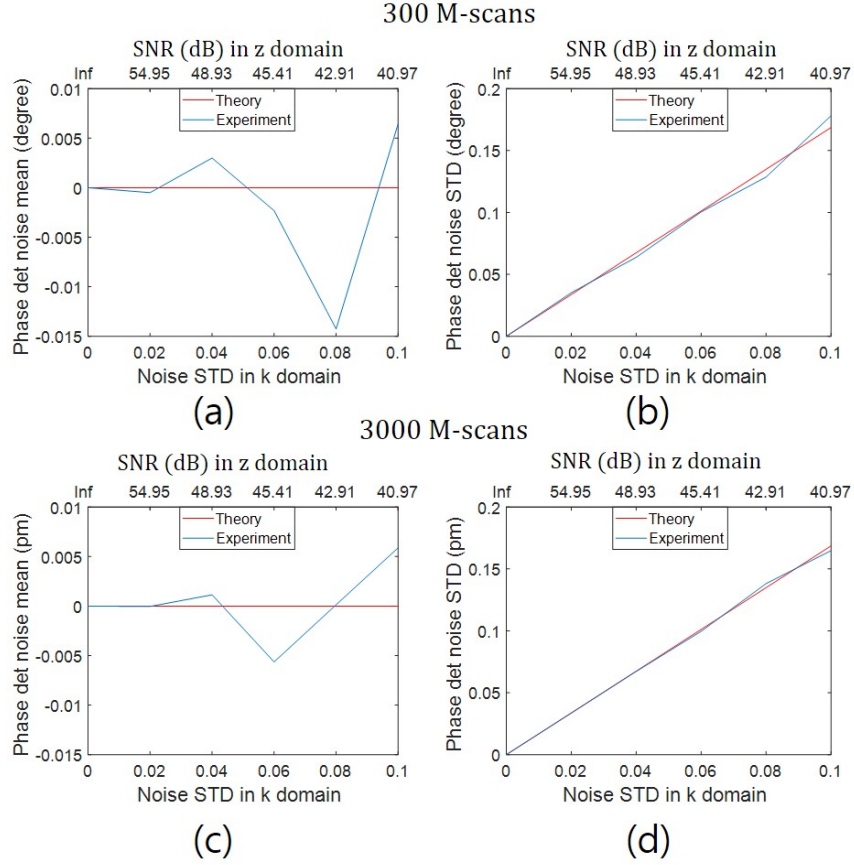
Figure 5.5: Comparison of statistical properties of phase detection noise. (a) and (b) are acquired from 300 measurements while (c) and (d) from 3000 measurements. (a), (c) and (b), (d) show comparison of phase detection noise mean and standard deviation, respectively. Red line means the result from Eq. (5.13) whereas blue one means from experimentally acquired detection noise.

noise and the statistical stationary state.

In order to verify Eq. (5.21) and Eq. (5.22), a set of interferograms were generated by assuming two reflectors. The interferogram of a reflector of interest was modeled using Eq. (5.14) such that $\rho S(k)\sqrt{R_R R_{S1}}/b = 1$, $\Delta z_1 = 1.713$ mm, $k_0 = 2\pi/1310$ nm, n = 1 to have the same specification as the one in Fig. 5.3(a). And the interferogram of an adjacent reflector was created in a way that has different intensity and axial position in z-domain such as $\rho S(k)\sqrt{R_R R_{S1}}/b = 1/3$ and $\Delta z_2 = 1.733$ mm.

Fig. 5.6(a) shows an interferogram with a pair of adjacent reflectors. The corresponding A-scan is shown in Fig. 5.6(b) where A-scans of total and each reflector are displayed with different
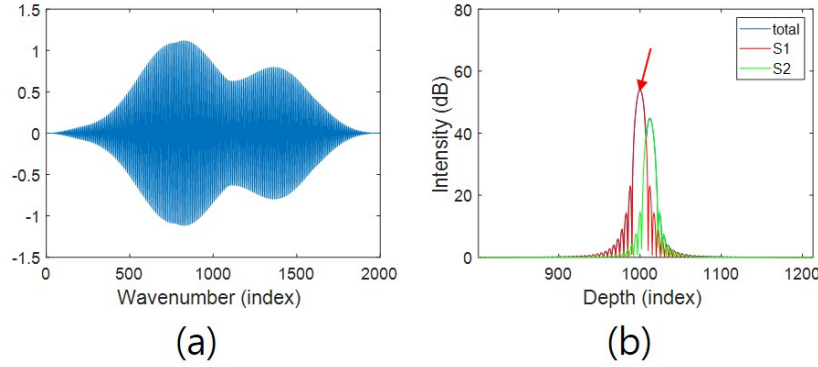
Figure 5.6: (a) One of modeled interferograms (b) A-scan of (a) where there are two signals: a reflector of interest (S1) and an adjacent one (S2). The vibrational signal of interest is extracted at the red arrow.

colors. For this A-scan, a zero padded 10,000 point FFT was used to better sample the reflectors, showing the side-bands which strongly overlap from both reflectors. The vibrational signal from S1 was chosen to have an amplitude, A_{vib} = 20 nm, and phase, θ_{vib} = 0 and 2000 time samples. The interferometric phase was extracted at the peak position of S1 as indicated by the red arrow in Eq. (5.6).

In order to observe the effect due to vibrational amplitude only, the vibrational amplitude of S2 was varied from 0 to 120 nm while keeping the vibrational phase the same as S1. Under these conditions the theoretical amplitude and phase detection errors as described in Eq. (5.21) and Eq. (5.22) are compared to simulated values as seen in Fig. 5.7. The simulated values were calculated by subtracting the ideal vibrational amplitude or phase from the measured one. In Fig. 5.7(a) and Fig. 5.7(b) the theoretical errors were calculated using non-approximated equation, Eq. (5.16). In Fig. 5.7(c) and Fig. 5.7(d), theoretical detection errors were calculated using approximated ones of Eq. (5.21) and Eq. (5.22). Both are shown to provide the reader with a sense of how the approximation holds up as vibrational amplitude of the adjacent reflector grows. As seen in Fig. 5.7(a) and Fig. 5.7 7(c), the displacement detection error decreases as the vibrational amplitude of S2 approaches the value of S1 (20 nm) and increases as the vibrational amplitude moves from the value of S1 up to 120 nm. This behavior was expected since Eq. (5.17) shows that when the vibrational

amplitude of neighboring reflectors are equal (i.e. $\delta z_1(t) = \delta z_2(t)$), there is no error in vibrational amplitude. As implied in Eq. (5.21), the measured vibrational amplitude comes closer to the expected one as the combined vibrational amplitude attenuates while the measured one goes away from the expected one, as the combined one rises. Phase detection errors are seen in Fig. 5.7(b) and Fig. 5.7(d) where theoretical and measured detections errors are zero. This is because the combined vibrational phase was kept the same as the expected one, making phase detection error zero as implied in Eq. (5.22).

Figure 5.7: Comparison of amplitude and phase detection errors in accordance with the vibrational amplitude of the adjacent reflector. Theoretical results in (a) and (b) are acquired using the non-approximated equation in Eq. (5.16) while (c) and (d) are acquired using the approximated equations in Eq. (5.21) and Eq. (5.22). (a), (c) and (b), (d) show comparison of amplitude and phase detection errors, respectively.

Next, the vibrational phase (θ_{vib}) of the adjacent reflector (S2) was swept from $0°$ to $180°$ while fixing the vibrational amplitude of it at 20 nm to see the effect of the vibrational phase of S2 only.

Fig. 5.8(a) and Fig. 5.8(b) displays results using the non-approximated equation of Eq. (5.16) while Fig. 5.8(c) and Fig. 5.8(d) shows using approximated equations of Eq. (5.21) and Eq. (5.22). The theoretical and experimental results in Fig. 5.8 were calculated in the same way as those in Fig. 5.7. As shown in Fig. 5.8(a) and Fig. 5.8(c), the displacement detection error (A_{error}) becomes larger as θ_{vib} of S2 increases. This result is related to the increase in the combined vibrational amplitude (A_{cvib}). When θ_{vib} of S2 is equal to zero, A_{cvib} becomes zero since the vibrational signal of S2 is the same as that of S1. This makes A_{error} zero by making the squared root term in Eq. (5.21) the same as the vibrational amplitude (A_{vib}) of S1. On the other hand, as θ_{vib} of S2 increases toward 180°, A_{cvib} is elevated and becomes two times larger than A_{vib} when θ_{vib} of S2 reaches 180°. This increase in A_{cvib} induces more displacement error by growing the square root term in Eq. (5.21) where the cosine term is negligible since G_{err} is as small as -2.763×10^{-3} in this simulation. Unlike the displacement detection error, the phase detection error θ_{error} increases as θ_{vib} of S2 moves from 0° to 90° whereas it decreases as θ_{vib} moves away from 90° towards 180° as seen in Fig. 5.8(b) and Fig. 5.8(d). This result can be explained with Eq. (5.22). When θ_{vib} of S2 changes from 0° to 90°, the cosine term in the denominator decreases while the sine term in the numerator increases, raising up θ_{error}. On the contrary, when θ_{vib} of S2 is swept from 90° to 180°, the cosine term increases while the sine term decreases, reducing θ_{error}. When θ_{vib} of S2 is equal to 90°, the maximum θ_{error} is achieved since cosine and sine terms become 1 and 0, respectively, as shown in Eq. (5.23).

5.4.2   Experimental Results

In order to verify the derived equations under normal experimental conditions, the movement of a piezo electric element was measured with a swept laser system described in [50]. The piezo was driven sinusoidally at 4 kHz and measured with A-scan (laser sweep) rate of 128.04 kHz over 50 ms, acquiring 6403 A-scans per M-scan. Two neutral density (ND) filters were used to change the incident light power on the piezo. Using this setup, A-scans with 3 different SNRs could be acquired by using no ND filter, 1 ND filter, or 2 ND filters. The resulting SNRs on the piezo were 57.89 dB, 48.81 dB, 21.21 dB, respectively. True vibrational amplitude and phase were estimated
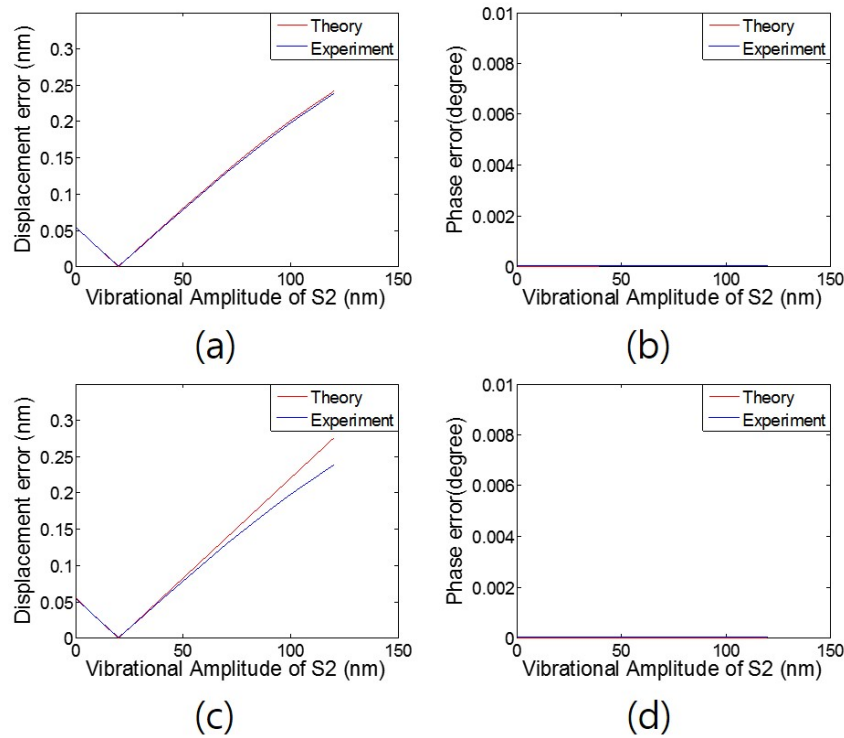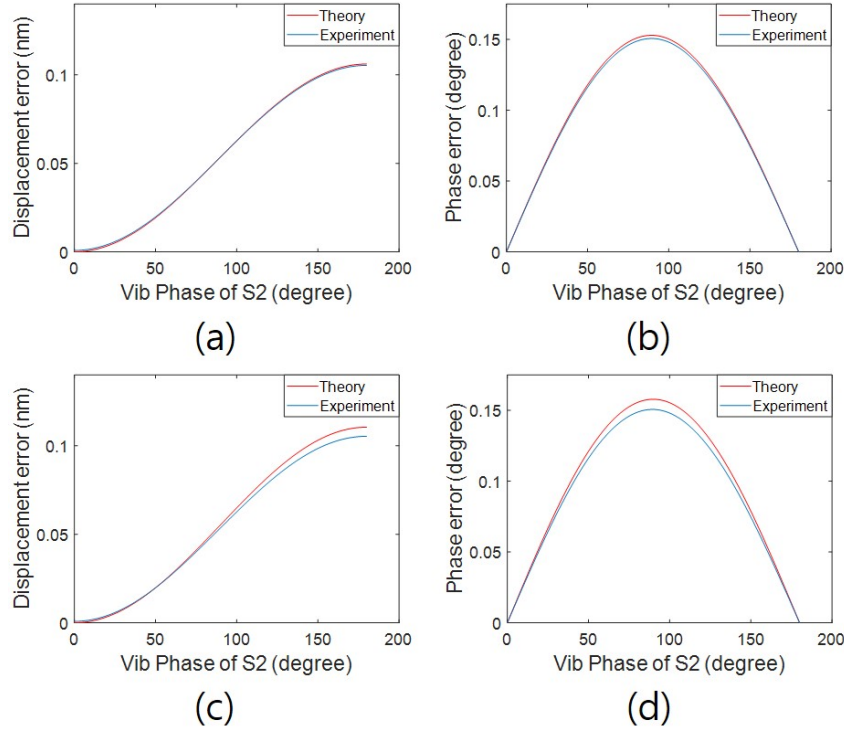
Figure 5.8: Comparison of amplitude and phase detection errors in accordance with the vibrational phase of the adjacent reflector. Theoretical results in (a) and (b) are acquired using the non-approximated equation in Eq. (5.16) while (c) and (d) are acquired using the approximated equations in Eq. (5.21) and Eq. (5.22). (a), (c) and (b), (d) show comparison of amplitude and phase detection errors, respectively.

by averaging 100 sets of M-scan data with the highest A-scan SNR (no ND filter) which are 2.788 nm and -144.556°, respectively.

Fig. 5.9 shows A-scans in root mean square (RMS) values and frequency domain vibrational responses from 100 M-scans measured with the piezo. And 1st, 2nd, and 3rd columns of Fig. 5.9 display results from the use of no ND, 1 ND and 2 ND filters, respectively. Fig. 5.9(d), Fig. 5.9(e), and Fig. 5.9(f) show frequency domain vibrational responses calculated from A-scans seen in Fig. 5.9(a), Fig. 5.9(b), and Fig. 5.9(c). To obtain frequency domain vibrational responses, time domain vibrational signals were extracted at peak locations red-arrowed in Fig. 5.9(a), Fig. 5.9(b), and Fig. 5.9(c). As can be seen in Fig. 5.9, the more ND filter is applied, the more the peak of the A-scan reduces and the farther it moves due to the increased optical pathlength caused by the

ND filter. Also, the RMS value of the frequency domain noise was acquired for each case with magnitudes ranging from 6 kHz to 10 kHz extracted along 100 M-scan data set by calculating $\sqrt{\mu^2 + \sigma^2}$ with their mean and standard deviation. It becomes higher such as 6.40 pm, 9.89 pm, and 288.44 pm shown in Fig. 5.9(d), Fig. 5.9(e), and Fig. 5.9(f), respectively.
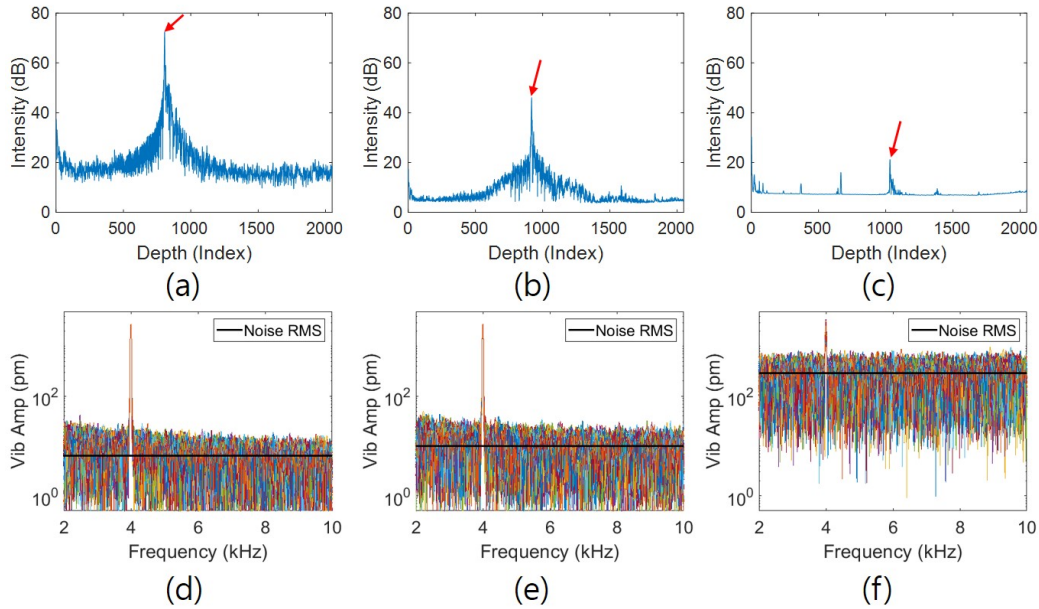
Figure 5.9: A-scans in root mean square (RMS) values and frequency domain vibrational responses measured from 100 M-scan with a piezo electric element driven by 4 kHz. (a) and (d) are A-scan and 100 frequency domain vibrational responses, respectively when no ND filter is used while (b), (e) and (c), (f) are from the use of 1 ND and 2 ND filters, respectively. In (d), (e), and (f), thick black line shows the RMS value of the frequency domain noise.

Experimental mean and standard deviation of amplitude and phase detection noises are calculated from the 3 sets of 100 M-scan data and compared to theoretical ones as displayed in Fig. 5.10. In this figure, experimental results follow the trend of theoretical ones, showing slightly larger values than them. To investigate the difference between theoretical and experimental results in Fig. 5.10 in more detail, the percentage errors of A_{noise} and θ_{noise} were calculated and displayed in Fig. 5.11. In this figure, the second moments or RMS values of those detection errors were used to derive errors in order to consider the mean and the standard deviation simultaneously.
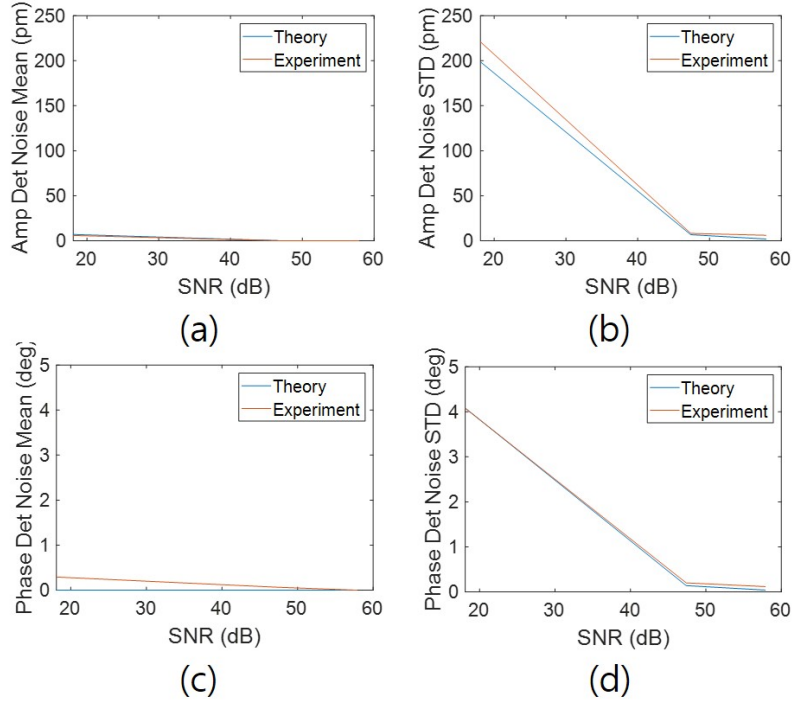
Figure 5.10: Mean and standard deviation of amplitude and phase detection noises in accordance with A-scan SNR. (a) and (b) show in pico meter scale mean and standard deviation of amplitude detection noise while (c) and (d) display in degree those of phase detection noise. Blue and red lines represent theoretical results calculated using Eq. (5.12) and Eq. (5.13), and experimentally measured ones, respectively.

It is shown in Fig. 5.11 that errors grow in accordance with the increase of SNR, meaning that experimental results are deviated more from theoretical ones. In this experiment, theoretical results were computed with SNR in z-domain since the SNR can be converted to the standard deviation of the time domain phase noise (σ_t). This means that theoretical results consider the noise existing in z-domain only which is transformed from k-domain. As seen in Fig. **??** (d) and Fig. **??** (e), however, other noise exists in the low frequency region while it is not seen in Fig. **??** (f). From this observation, it can be thought that additive noise in k-domain is dominant when SNR is low whereas other noise residing in an interferometric phase has more effect when SNR is high, causing more deviation of experimental results from theoretical ones.

Therefore, the piezo experiment with an OCT vibrometry system demonstrated that the derived equations work well within the assumption of additive noise in k-domain while they show more
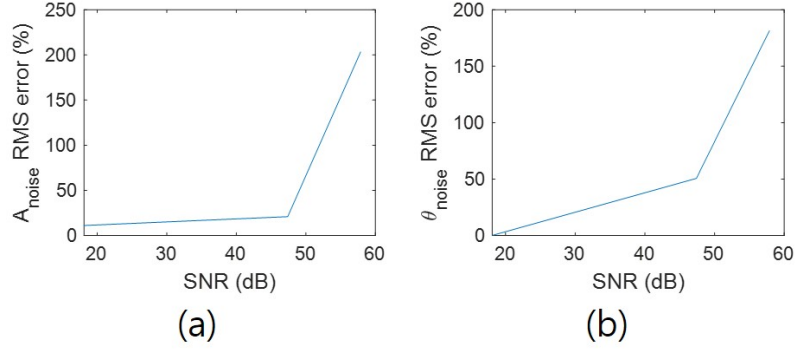
Figure 5.11: RMS errors of amplitude and phase detection noises in accordance with A-scan SNR. (a) and (b) show percentage errors of amplitude detection noise and phase detection noise, respectively. RMS error was calculated by $|TheoreticalRMS - ExperimentalRMS|/TheoreticalRMS \times 100$ where RMS was computed by the square root of mean squared plus standard deviation squared.

error when other noise is added to an interferometric phase.

The derived detection errors of an adjacent reflector were verified with the same OCT system and piezo as those used for additive noise. In this setup, the vibration of the piezo was measured with 4 kHz stimulus at two different depths: one is for the reflector of interest and the other is for the adjacent one. And then the measured data with different depths were added together because exact vibrational amplitudes and phases of interesting and neighboring reflectors are required to use derived equations. Also, different voltages were applied to the piezo for the adjacent reflector to vibrate around 1, 9, and 36 times larger than the interesting one. To minimize the effect of additive noise, 100 trials of M-scan data were acquired for each measurement and then averaged along the trial number to generate one M-scan.

Fig. 5.12(a), Fig. 5.12(b), and Fig. 5.12(c) show A-scans averaged along time from the generated M-scan data. From the peak location shown in violet lines in Fig. 5.12(a), Fig. 5.12(b), and Fig. 5.12(c), time domain vibrational signals were extracted and transformed to frequency domain vibrational responses as seen in Fig. 5.12(d), Fig. 5.12(e), and Fig. 5.12(f)

Theoretical amplitude and phase detection errors in Eq. (5.21) and Eq. (5.22) were calculated with required parameters obtained from A-scans and vibrational signals shown in Fig. 5.12. And it

68
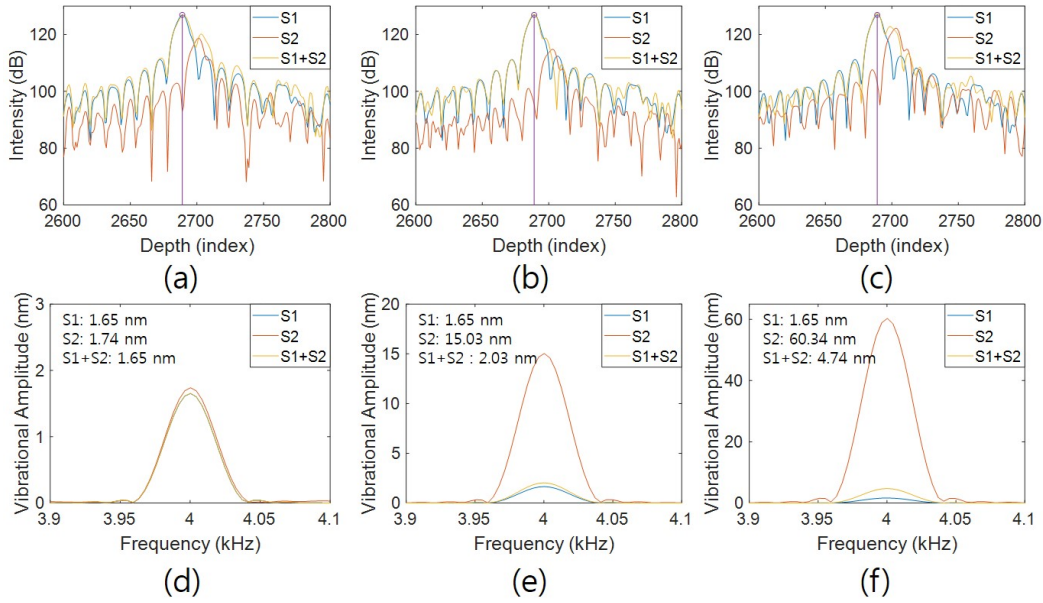
Figure 5.12: Averaged A-scans and frequency domain vibrational responses measured with a piezo electric element driven by 4 kHz. (a), (b) and (c) display A-scans while (d), (e), and (f) show frequency domain vibrational responses. Left, middle, and right columns are acquired when an adjacent reflector is stimulated to vibrate around 1, 9, 36 times larger than the reflector of interest, respectively. The interesting reflector (S1), the adjacent reflector (S2), and combined one (S1+S2) are shown with blue, red, and yellow colors, respectively. Also, measured vibrational amplitudes are displayed in (d), (e), and (f).

is compared to experimental ones as seen in Fig. 5.13. When the ratios of the vibrational amplitude of S2 to S1 are between 0 and 10, theoretical errors look similar or slight different compared to experimental ones. However, more difference are shown when the ratio is around 36. This is because, as explained in Simulation Result section, the combined vibrational amplitude increases in accordance with that of S2, making approximated equations deviate more from non-approximated ones. Therefore, Eq. (5.21) and Eq. (5.22) work well with the case when the ratio of the vibrational amplitude of S2 to S1 is not high while Eq. (5.17) is preferred in other cases.
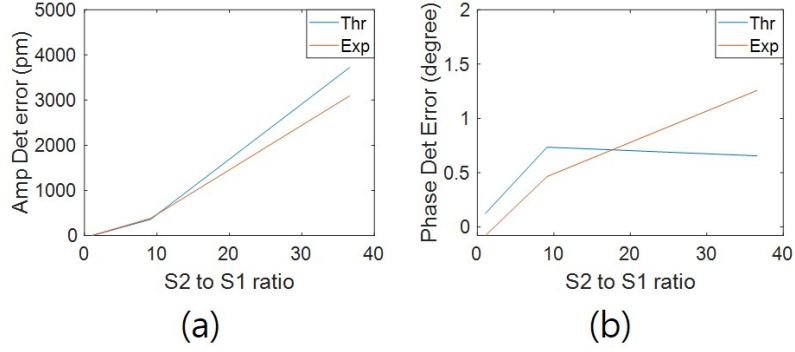
Figure 5.13: Amplitude and phase detection errors in accordance with the ratio of the vibrational amplitude of S2 to S1. (a) and (b) show amplitude and phase detection errors, respectively. Blue line represents theoretical results calculated using Eq. (5.21) and Eq. (5.22) while red line is for experimentally measured ones.

5.5   Discussion

5.5.1   Sensitivity

The sensitivity of OCT for vibrometry is clearly tied to the signal to noise ratio of the OCT system, i.e. $\sigma_t = (2SNR)^{-1/2}$. The ultimate limit to the OCT system SNR is shot-noise, $\sigma_k = (2\rho R_r SB)^{1/2}$, where B is the noise equivalent bandwidth and S is the source average power. Using the magnitude of Eq. (5.2) and recognizing that $s(0) = NS$ for an ideal flat-top laser power profile, the SNR can be shown to be, $(|h(z)|/E[|n(z)|^2] = N\rho SR_s/(4b^2 B))$. This is equivalent to the result in [13] for b=1. Assuming an anti-aliasing filter has been used, then B is half of the sampling frequency and the SNR can be rewritten in terms of the sweep frequency (f_{sweep}) and duty cycle (D) or sweep time (Δt),

$$SNR = \frac{\rho SR_s}{2b^2} \frac{D}{f_{sweep}} = \frac{\rho SR_s}{2b^2} \Delta t \qquad (5.24)$$

A similar equation can be derived for spectrometer based systems [13, 12, 14] where Δt is the camera integration time. The SNR of the OCT system goes up with higher power on the sample (S↑) and slower sweep rate (higher integration time, Δt ↑), hence the sensitivity of the vibrometer improves as well. For every 10 dB improvement in the system SNR, the time-domain phase noise,

$n_t(t)$, is reduced by $1/\sqrt{10}$ for a 3 fold improvement. Equivalently, for a 3-fold improvement in s/n, the phase noise is reduced by 1/3.

While we have focused on revealing the statistical properties of the signals in OCT based vibrometry we have not directly addressed sensitivity. In our work [2, 51, 52] we typically use $\mu_{fR} + 3\sigma_{fR}$ as a threshold. In other words, any signal below this threshold is neglected. This metric has the advantage that it can readily be measured in each acquisition by considering the mean and standard deviation in a frequency region near the stimulus frequency and it corresponds to 98% confidence interval of the Rayleigh distribution. In terms of the relationships of Fig. 5.1 the sensitivity is,

$$ sens = \mu_{fR} + 3\sigma_{fR} = \left(\frac{\sqrt{\pi} + 3\sqrt{4 - \pi}}{4k_0 n} \right) (M \cdot SNR)^{-1/2} \tag{5.25} $$

where M, the number of time samples, and SNR are the only variables for a given system.

For every 100 fold increase in M, the sensitivity is improved by a factor of 10. Likewise a 20 dB improvement in SNR, improves the sensitivity by a factor of 10. If we consider the shot noise limit, Eq. (5.24) can be substituted into Eq. (5.25) to get

$$ sens = \left(\frac{\sqrt{\pi} + 3\sqrt{4 - \pi}}{4k_0 n} \right) \sqrt{\frac{2b^2}{\rho S R_s \Delta t M}} \tag{5.26} $$

Fundamentally, an increase in the sample reflectivity (R_s) or the total acquisition time ($\Delta t M$) improves the system sensitivity. Likewise there is a fundamental advantage to using a shorter wavelength of light (larger k_0) for vibrometry. Obviously, that advantage is offset by the larger scattering cross-section at shorter wavelengths which will result in lower SNR at depth in the tissue.

OCT systems are commonly specified by the signal to noise ratio expected for a perfect reflector ($R_s = 1$) on a decibel scale. For instance, the maximum SNR of the swept laser system used to collect the data above was 107 dB. The theoretical shot-noise limit was 110 dB. Developing a similar metric for vibrometry performance would be helpful in comparing systems with different

architectures and newly developed algorithms for extracting the vibratory response. Assuming n=M=1 and using Eq. (5.25) and Eq. (5.26), this system has a potential sensitivity of 8.4 pm based on measured SNR and 5.9 pm in the shot-noise limit. Tissue reflectivity is typically in the range of -40 to -80 dB, hence in order to realize the 8.4 pm sensitivity M would need to be set in the range $10^4 \sim 10^8$. For our 128.04 kHz system, that corresponds to an acquisition time of 78 ms – 13 min.

5.5.2 Impact of system vibration and motion artifact

Small changes in the optical pathlength due to a wide range of sources, e.g. air-currents and building vibrations, introduce phase-noise to the system. These tend to be concentrated in the low frequency range, producing an 1/f dependence. Obviously, this deviates from our assumption of Gassian white noise, however at some frequency, the mean and standard deviation will become approximately constant with increasing frequency. For our system that limit is 2 kHz, as shown above. Beyond this limit our experimental measures match well with the derived equations because the noise is approximately Gaussian white. It is possible to suppress this low frequency phase noise using an interferometer where the reference and sample arm largely co-propagate so that the small scale vibrations are common to both, i.e. a common mode interferometer. Larger scale changes in the optical pathlength can be introduced by patient/sample motion during data acquisition. Again, this will introduce phase-noise and could violate the condition of a stationary state utilized in the derivation of noise statistics. As we have noted elsewhere, [50] under these circumstances, a broad band increase in phase-noise can be observed, however time-domain averaging of the interferometric phase substantially lowers the phase-noise since the motion artifact is incoherent.

5.5.3 Impact of windowing

A window function is typically used in an OCT vibrometry to reduce sidelobes of other frequency components. This is because these sidelobes can deviate vibrational amplitude and phase of the frequency component of interest when they are strong. For this purpose, a window function is applied to the time domain phase signal in Eq. (5.7) and has an impact on statistical properties of amplitude and phase detection noises since it changes intensities of signal and noise in the time

domain. Considering the effect of the window function, Eq. (5.11) is expressed as

$$\sqrt{E[A_{noise}^2]} = \sqrt{\frac{E_w \sigma_t^2}{2k_0^2 n^2 W^2(0)}} = \frac{\sigma_t \sqrt{E_w}}{k_0 n W(0)} \tag{5.27a}$$

$$\sqrt{E[A_{noise}^2]} = \frac{1.225 \sigma_t}{k_0 n \sqrt{M}} \; for \; hanning \; window \tag{5.27b}$$

where E_w is the total energy of the window function calculated from $E_w = \sum_{i=1}^{M} w^2(t_i)$ and W(0) is the DC component of W(f) calculated from $W_0 = \sum_{i=1}^{M} w(t_i)$.

Eq. (5.27a) shows the second moment of A_{noise} for general case while Eq. (5.27b) displays when hanning window is used. Compared to Eq. (5.11), the second moment of using the hanning window increases by 1.225 times because the energy of the interesting phase signal ($2k_0 n \delta z(t)$) is reduced more than that of the time domain phase noise ($n_t(t)$) by the hanning window. Statistical properties of A_{noise} and θ_{noise} are easily converted by replacing M with $W^2(0)/E_w$.

5.5.4 Equivalence of measuring the phase noise as a function of frequency or time

It is shown from the derivation that the time domain phase noise ($n_t(t)$) in Eq. (5.7) is white Gaussian and the magnitude of the frequency domain noise ($n_f(f)$) is Rayleigh distributed when A_{vib} is equal to 0. Since the noise energy is preserved between these domains, their second moments have the relationship of $E[n_t^2(t)] = 1/M * E[n_f^2(f)]$, meaning that $E[n_f^2(f)]$ can be predicted by calculating $E[n_t^2(t)]$. This relationship assumes that other noise sources that induce small changes in the optical pathlength are not included. Thus, it is important to process data to reduce the effects of other noise sources not only to have the consistent relationship between $n_t(t)$ and $n_f(f)$ but also to increase measurement accuracy.

The preprocessing (second step in Fig. 5.1) typically done is the subtraction of a background signal to remove the constant term, which will appear at z=0. The side-lobes from a strong signal at z=0 can sometimes overlap with signals of interest. We typically measure the background as the mean over a large number of acquisitions and bandpass filter. It is essentially noise free and therefore does not appreciably contribute to the noise. We also typically preprocess the time-

domain phase, $\phi(z,t)$, before calculating the Fourier transform to get $\phi(z,f)$. At a minimum we calculate and then subtract the mean of $\phi(z,t)$, to suppress the signal at 0 Hz. This approach is fast and does not contribute to the noise above 0 Hz. In post-processing where computational time is not critical, we sometimes will instead fit $\phi(z,t)$ to a polynomial and subtract the fit from $\phi(z,t)$. This suppresses the signal at 0 Hz and removes some of the low frequency drift again without introducing noise. Some researchers have taken the derivative by computing $\Delta\phi(z,t) = \phi(z,t_2) - \phi(z,t_1)$. This similarly removes the 0 Hz portion of the signal, however it introduces an additional $\sqrt{2}$ noise so that $\sigma_t = (4SNR)^{-1/2}$.

5.5.5 How to reduce the effect of additive noise

From now on, methods to reduce those effects are discussed where it is assumed that a laser source is given since it depends on an application. In order to reduce the effect of additive noise, the amount of the noise should be reduced above all. In a simple way, this can be achieved by selectively attenuating the reference arm power in an interferometer because it allows the noise to be close to shot noise limit while reducing RIN [43]. Also, balanced detection can be adopted with Mach-Zehnder interferometer to suppress RIN [53]. Secondly, the effect of additive noise can be attenuated by raising time duration for M-scan. This means increase in M in Eq. (5.11), diminishing amplitude and phase detection noise. Finally, it can be helpful to acquire multiple M-scans at the same location to average time domain phase signal in Eq. (5.7). This is because averaging forces the time domain phase noise $n_t(t)$ in Eq. (5.7) to approach zero. However, the second and the third methods requires careful selection of the duration time and the number of M-scans depending on a sample. If a sample is stationary, the duration time and the number can be easily determined depending on an experimental environment. On the other hand, if a sample moves in a way that its axial location changes, this movement induces artifacts in A-scans which deteriorates extraction of time domain phases. Therefore, it is important to optimize those parameters for this type of sample.

5.5.6 How to reduce the effect of an adjacent reflector

Reducing the effect of an adjacent reflector can be simplified to decreasing the relative magnitude of an adjacent reflector over an interesting one, $|s(\Delta z_{1-2})|/|s(0)|$ as shown in Eq. (5.16). This means that the effect is not related to M and k_0 in Eq. (5.11), exhibiting the difference from the effect of additive noise. Lowering $|s(\Delta z_{1-2})|/|s(0)|$ is achieved by selecting a widow function carefully to be multiplied to acquired interferograms. For this purpose, the use a rectangular window should be avoided since it has the largest sidelobes compared to others [33]. The commonly used window function in measuring mechanical responses of a sample with OCT is hanning window [2, 54, 55]. This is from the fact that not only has hanning window the lower first sidelobes but also the other sidelobes decrease progressively along depth [33]. Along with careful section of a window function, it is recommended to pick a vibrational signal at the peak of reflector of interest since the relative magnitude is usually low at this point [42]. An additional advantage of selecting the peak signal is that the effect of additive noise is reduced due to high SNR.

5.6 Conclusion

In this article the effects of additive noise and adjacent reflectors are analyzed to investigate how they affect detecting vibrational amplitude and phase in the frequency domain. For this purpose, time domain phase noise and time domain phase error are separated from time domain phase signal to see their effects only.

The derived equations were checked with MATLAB simulation and then verified with a piezo electric element using a swept-source OCT system. The results show that derived equations allow the effects of additive noise and an adjacent reflector to be predicted when detecting vibrational amplitude and phase in the frequency domain. Also, those equations provide theoretical support to find methods that reduce those effects. Either can be used for reducing the effect of additive noise with a given laser, to increase the number of A-scan for one M-scan or to average time domain phase signals by acquiring many M-scans as well as optimizing the reference arm power. And careful design of windowing is required to reduce the effect of an adjacent reflector by in-

creasing the relative magnitude of the reflector of interest over the adjacent one. In conclusion, the derivation in this chapter allows for predicting the performance of an OCT vibrometry system in measuring vibrational amplitude ans phase, and for figuring out ways to reduce those inherent effects theoretically.

6. SUMMARY AND CONCLUSIONS

In this work, we tackled three main problems that hindered the use of swept-source OCT (SSOCT) based vibrometry. The SSOCT based vibrometry has advantages in acquisition speed and imaging depth over spectral-domain OCT (SDOCT) which originates from features of a swept-laser source such as fast sweep rate and long coherence length. In spite of those benefits, the swept-laser source suffers problems: non-linear wavenumber sweeping, and different starting wavenumber between sweepings called intra - and inter-sweep variability, respectively. This was the problem we addressed at first because the most important features, such as image quality and displacement sensitivity, were not guaranteed without solving this issue. To deal with this problem, we proposed complex FIR based spectral calibration to calibrate every sweep of the interferogram in real time. In this method, every swept wavenumber was extracted from a reference signal and used to calibrate the OCT signals to have the same linear wavenumber for removing intra- and inter-sweep variability. The method was compared to the traditional IFFT-FFT based spectral calibration. The results showed that the proposed approach required less hardware resources in FPGA and demonstrated as good or slightly better results on OCT image quality and displacement sensitivity. Also, we explored compensating chromatic variation from a laser source with the magnitude of a reference signal extracted from the complex FIR based approach. And the result showed that this method could correct the variation in real time, suggesting its usefulness for a laser suffering chromatic variation. Therefore, the complex FIR based method removes inherent problems in swept-laser sources effectively and efficiently, expanding the use of swept-source OCT for functional imaging.

After solving the swept-laser issue, the next problem that needed to be addressed was the significant increase in processing time. This problem occurs due to the considerable amount of required data and the longer processing steps needed to obtain volumetric, structural and vibrational image. To deal with this problem, an efficient acquisition scheme was proposed along with a method to reduce processing time. In the acquisition scheme, the Alazartech card was exploited to acquire new

data while transferring previous one to host. Also, processing time was reduced by implementing on GPU so that the total time of transfer and processing was within acquisition time, allowing efficient use of the Alazartech card memory. The proposed method was applied to perform a single point M-scan, BM-scan, and volume M-scan in order to obtain additional vibrational and structural information at one axial point (z-axis), over two dimensions (x, z), and over three dimensions (x, y, z), respectively. And it was demonstrated that a series of M-scan data were acquired and processed in near real time, showing only a little latency slightly less than acquisition time. Therefore, it can provide biologists and clinicians with structural and vibrational information at a single point, over a B-scan region or over a volume region with improved throughputs. In addition, it can be applicable to functional imaging that garners interferometric phases such as Doppler OCT and OCT elastography.

The last issue that we faced was determining how to theoretically analyze the effects of additive noise and adjacent reflectors, inherent in OCT vibrometry, on measuring vibrational amplitude and phase. This analysis was important because it was able to provide theoretical supports to evaluate the performance of an OCT vibrometry system and to find methods to reduce measurement errors. In the analysis, phase noise and phase error caused by additive noise and an adjacent reflector were separated from the phase signal of interest which was converted to a vibrational signal by scaling. This separation allowed us to easily figure out how phase noise and phase error affect the detection of a vibrational signal in the frequency domain. The derived equations were checked with MATLAB simulation and then verified with a piezo electric element using a swept-source OCT system. It was shown that results from derived equations matched well with those from experiments, suggesting they can be used to predict the performance of a system. In addition, they provided a theoretical framework to find methods that reduce those effects. Either it can be used for reducing the effect of additive noise with a given laser, to increase the number of A-scans for one M-scan or to average the time domain phase signals by acquiring many M-scans. Also it is required to optimize the reference arm power for achieving an optimal SNR with a given laser power. Whereas, careful design of windowing is required to reduce the effect of an adjacent

reflector by increasing the relative magnitude of the reflector of interest over the adjacent one. This analysis is not restricted to the field of OCT vibrometry. It can be applied to imaging methods that exploit interferometric phases.

REFERENCES

[1] E. W. Chang, J. T. Cheng, C. Röösli, J. B. Kobler, J. J. Rosowski, and S. H. Yun, "Simultaneous 3d imaging of sound-induced motions of the tympanic membrane and middle ear ossicles," *Hearing research*, vol. 304, pp. 49–56, 2013.

[2] H. Y. Lee, P. D. Raphael, J. Park, A. K. Ellerbee, B. E. Applegate, and J. S. Oghalai, "Noninvasive in vivo imaging reveals differences between tectorial membrane and basilar membrane traveling waves in the mouse cochlea," *Proceedings of the National Academy of Sciences*, p. 201500038, 2015.

[3] J. Kim, A. Xia, N. Grillet, B. E. Applegate, and J. S. Oghalai, "Osmotic stabilization prevents cochlear synaptopathy after blast trauma," *Proceedings of the National Academy of Sciences*, p. 201720121, 2018.

[4] S. S. Gao, R. Wang, P. D. Raphael, Y. Moayedi, A. K. Groves, J. Zuo, B. E. Applegate, and J. S. Oghalai, "Vibration of the organ of corti within the cochlear apex in mice," *Journal of neurophysiology*, vol. 112, no. 5, pp. 1192–1204, 2014.

[5] C. T. Nguyen, H. Tu, E. J. Chaney, C. N. Stewart, and S. A. Boppart, "Non-invasive optical interferometry for the assessment of biofilm growth in the middle ear," *Biomedical optics express*, vol. 1, no. 4, pp. 1104–1116, 2010.

[6] H. M. Subhash, S. L. Jacques, A. T. Nguyen-Huynh, A. L. Nuttall, R. K. Wang, and N. Choudhury, "Feasibility of spectral-domain phase-sensitive optical coherence tomography for middle ear vibrometry," *Journal of biomedical optics*, vol. 17, no. 6, p. 060505, 2012.

[7] W. Choi, B. Potsaid, V. Jayaraman, B. Baumann, I. Grulkowski, J. J. Liu, C. D. Lu, A. E. Cable, D. Huang, J. S. Duker, *et al.*, "Phase-sensitive swept-source optical coherence tomography imaging of the human retina with a vertical cavity surface-emitting laser light source," *Optics letters*, vol. 38, no. 3, pp. 338–340, 2013.

[8] M. Gora, K. Karnowski, M. Szkulmowski, B. J. Kaluzny, R. Huber, A. Kowalczyk, and M. Wojtkowski, "Ultra high-speed swept source oct imaging of the anterior segment of human eye at 200 khz with adjustable imaging range," *Optics Express*, vol. 17, no. 17, pp. 14880–14894, 2009.

[9] B. Baumann, B. Potsaid, M. F. Kraus, J. J. Liu, D. Huang, J. Hornegger, A. E. Cable, J. S. Duker, and J. G. Fujimoto, "Total retinal blood flow measurement with ultrahigh speed swept source/fourier domain oct," *Biomedical optics express*, vol. 2, no. 6, pp. 1539–1552, 2011.

[10] B. Braaf, K. A. Vermeer, V. A. D. Sicam, E. van Zeeburg, J. C. van Meurs, and J. F. de Boer, "Phase-stabilized optical frequency domain imaging at 1-μm for the measurement of blood flow in the human choroid," *Optics express*, vol. 19, no. 21, pp. 20886–20903, 2011.

[11] A. F. Fercher, C. K. Hitzenberger, G. Kamp, and S. Y. El-Zaiat, "Measurement of intraocular distances by backscattering spectral interferometry," *Optics communications*, vol. 117, no. 1-2, pp. 43–48, 1995.

[12] R. Leitgeb, C. Hitzenberger, and A. F. Fercher, "Performance of fourier domain vs. time domain optical coherence tomography," *Optics express*, vol. 11, no. 8, pp. 889–894, 2003.

[13] M. A. Choma, M. V. Sarunic, C. Yang, and J. A. Izatt, "Sensitivity advantage of swept source and fourier domain optical coherence tomography," *Optics express*, vol. 11, no. 18, pp. 2183–2189, 2003.

[14] J. F. De Boer, B. Cense, B. H. Park, M. C. Pierce, G. J. Tearney, and B. E. Bouma, "Improved signal-to-noise ratio in spectral-domain compared with time-domain optical coherence tomography," *Optics letters*, vol. 28, no. 21, pp. 2067–2069, 2003.

[15] M. V. Sarunic, M. A. Choma, C. Yang, and J. A. Izatt, "Instantaneous complex conjugate resolved spectral domain and swept-source oct using $3\times$ 3 fiber couplers," *Optics express*, vol. 13, no. 3, pp. 957–967, 2005.

[16] Y. Wang, B. A. Bower, J. A. Izatt, O. Tan, and D. Huang, "In vivo total retinal blood flow measurement by fourier domain doppler optical coherence tomography," *Journal of biomedical optics*, vol. 12, no. 4, p. 041215, 2007.

[17] Y. Zhao, Z. Chen, C. Saxer, S. Xiang, J. F. de Boer, and J. S. Nelson, "Phase-resolved optical coherence tomography and optical doppler tomography for imaging blood flow in human skin with fast scanning speed and high velocity sensitivity," *Optics letters*, vol. 25, no. 2, pp. 114–116, 2000.

[18] R. A. Leitgeb, L. Schmetterer, W. Drexler, A. Fercher, R. Zawadzki, and T. Bajraszewski, "Real-time assessment of retinal blood flow with ultrafast acquisition by color doppler fourier domain optical coherence tomography," *Optics Express*, vol. 11, no. 23, pp. 3116–3121, 2003.

[19] J. M. Schmitt, "Oct elastography: imaging microscopic deformation and strain of tissue," *Optics express*, vol. 3, no. 6, pp. 199–211, 1998.

[20] J. Rogowska, N. Patel, J. Fujimoto, and M. Brezinski, "Optical coherence tomographic elastography technique for measuring deformation and strain of atherosclerotic tissues," *Heart*, vol. 90, no. 5, pp. 556–562, 2004.

[21] B. E. Applegate, R. L. Shelton, S. S. Gao, and J. S. Oghalai, "Imaging high-frequency periodic motion in the mouse ear with coherently interleaved optical coherence tomography," *Optics letters*, vol. 36, no. 23, pp. 4716–4718, 2011.

[22] S. S. Gao, P. D. Raphael, R. Wang, J. Park, A. Xia, B. E. Applegate, and J. S. Oghalai, "In vivo vibrometry inside the apex of the mouse cochlea using spectral domain optical coherence tomography," *Biomedical optics express*, vol. 4, no. 2, pp. 230–240, 2013.

[23] B. Potsaid, B. Baumann, D. Huang, S. Barry, A. E. Cable, J. S. Schuman, J. S. Duker, and J. G. Fujimoto, "Ultrahigh speed 1050nm swept source/fourier domain oct retinal and anterior segment imaging at 100,000 to 400,000 axial scans per second," *Optics express*, vol. 18, no. 19, pp. 20029–20048, 2010.

[24] C. Azeredo-Leme, "Clock jitter effects on sampling: A tutorial," *IEEE Circuits and Systems Magazine*, vol. 11, no. 3, pp. 26–37, 2011.

[25] R. Huber, M. Wojtkowski, K. Taira, J. G. Fujimoto, and K. Hsu, "Amplified, frequency swept lasers for frequency domain reflectometry and oct imaging: design and scaling principles," *Optics Express*, vol. 13, no. 9, pp. 3513–3528, 2005.

[26] B. Vakoc, S. Yun, J. De Boer, G. Tearney, and B. Bouma, "Phase-resolved optical frequency domain imaging," *Optics express*, vol. 13, no. 14, pp. 5483–5493, 2005.

[27] A. Reilly, G. Frazer, and B. Boashash, "Analytic signal generation-tips and traps," *IEEE Transactions on Signal Processing*, vol. 42, no. 11, pp. 3241–3245, 1994.

[28] K. Ayob, *Digital Filters in Hardware: A Practical Guide for Firmware Engineers*. digital filters, 2008.

[29] L. Thrane, H. E. Larsen, K. Norozi, F. Pedersen, J. B. Thomsen, M. Trojer, and T. M. Yelbuz, "Field programmable gate-array-based real-time optical doppler tomography system for in vivo imaging of cardiac dynamics in the chick embryo," *Optical Engineering*, vol. 48, no. 2, p. 023201, 2009.

[30] P. Levesque and M. Sawan, "Real-time hand-held ultrasound medical-imaging device based on a new digital quadrature demodulation processor," *IEEE transactions on ultrasonics, ferroelectrics, and frequency control*, vol. 56, no. 8, 2009.

[31] H. E. Larsen, R. T. Nilsson, L. Thrane, F. Pedersen, T. M. Jørgensen, and P. E. Andersen, "Optical doppler tomography based on a field programmable gate array," *Biomedical Signal Processing and Control*, vol. 3, no. 1, pp. 102–106, 2008.

[32] P. K. Meher, J. Valls, T.-B. Juang, K. Sridharan, and K. Maharatna, "50 years of cordic: Algorithms, architectures, and applications," *IEEE Transactions on Circuits and Systems I: Regular Papers*, vol. 56, no. 9, pp. 1893–1907, 2009.

[33] B. Porat, *A course in digital signal processing*. John Wiley & Sons, Inc., 1996.

[34] A. E. Desjardins, B. J. Vakoc, M. J. Suter, S.-H. Yun, G. J. Tearney, and B. E. Bouma, "Real-time fpga processing for high-speed optical frequency domain imaging," *IEEE transactions on medical imaging*, vol. 28, no. 9, pp. 1468–1472, 2009.

[35] J. Park, E. F. Carbajal, X. Chen, J. S. Oghalai, and B. E. Applegate, "Phase-sensitive optical coherence tomography using an vernier-tuned distributed bragg reflector swept laser in the mouse middle ear," *Optics letters*, vol. 39, no. 21, pp. 6233–6236, 2014.

[36] M. Szkulmowski, I. Grulkowski, D. Szlag, A. Szkulmowska, A. Kowalczyk, and M. Wojtkowski, "Flow velocity estimation by complex ambiguity free joint spectral and time domain optical coherence tomography," *Optics express*, vol. 17, no. 16, pp. 14281–14297, 2009.

[37] A. K. Ellerbee and J. A. Izatt, "Phase retrieval in low-coherence interferometric microscopy," *Optics letters*, vol. 32, no. 4, pp. 388–390, 2007.

[38] M. A. Choma, A. K. Ellerbee, C. Yang, T. L. Creazzo, and J. A. Izatt, "Spectral-domain phase microscopy," *Optics letters*, vol. 30, no. 10, pp. 1162–1164, 2005.

[39] C. Joo, T. Akkin, B. Cense, B. H. Park, and J. F. De Boer, "Spectral-domain optical coherence phase microscopy for quantitative phase-contrast imaging," *Optics letters*, vol. 30, no. 16, pp. 2131–2133, 2005.

[40] M. Szkulmowski, A. Szkulmowska, T. Bajraszewski, A. Kowalczyk, and M. Wojtkowski, "Flow velocity estimation using joint spectral and time domain optical coherence tomography," *Optics Express*, vol. 16, no. 9, pp. 6008–6025, 2008.

[41] H. Gudbjartsson and S. Patz, "The rician distribution of noisy mri data," *Magnetic resonance in medicine*, vol. 34, no. 6, pp. 910–914, 1995.

[42] N. C. Lin, C. P. Hendon, and E. S. Olson, "Signal competition in optical coherence tomography and its relevance for cochlear vibrometry," *The Journal of the Acoustical Society of America*, vol. 141, no. 1, pp. 395–405, 2017.

[43] W. V. Sorin and D. M. Baney, "A simple intensity noise reduction technique for optical low-coherence reflectometry," *IEEE Photonics Technology Letters*, vol. 4, no. 12, pp. 1404–1406, 1992.

[44] B. M. Hoeling, A. D. Fernandez, R. C. Haskell, E. Huang, W. R. Myers, D. C. Petersen, S. E. Ungersma, R. Wang, M. E. Williams, and S. E. Fraser, "An optical coherence microscope for 3-dimensional imaging in developmental biology," *Optics Express*, vol. 6, no. 7, pp. 136–146, 2000.

[45] P. Morkel, R. Laming, and D. Payne, "Noise characteristics of high-power doped-fibre super-luminescent sources," *Electronics Letters*, vol. 26, no. 2, pp. 96–98, 1990.

[46] M. A. Richards, "The discrete-time fourier transform and discrete fourier transform of windowed stationary white noise," *Georgia Institute of Technology, Tech. Rep*, 2013.

[47] A. Papoulis and S. U. Pillai, *Probability, random variables, and stochastic processes*. Tata McGraw-Hill Education, 2002.

[48] D. J. Inman, *Vibration with control*. Wiley, 2006.

[49] R. L. Warren, S. Ramamoorthy, N. Ciganović, Y. Zhang, T. M. Wilson, T. Petrie, R. K. Wang, S. L. Jacques, T. Reichenbach, A. L. Nuttall, *et al.*, "Minimal basilar membrane motion in low-frequency hearing," *Proceedings of the National Academy of Sciences*, vol. 113, no. 30, pp. E4304–E4310, 2016.

[50] W. Kim, S. Kim, J. S. Oghalai, and B. E. Applegate, "Endoscopic optical coherence tomography enables morphological and subnanometer vibratory imaging of the porcine cochlea through the round window," *Optics letters*, vol. 43, no. 9, pp. 1966–1969, 2018.

[51] H. Y. Lee, P. D. Raphael, A. Xia, J. Kim, N. Grillet, B. E. Applegate, A. K. E. Bowden, and J. S. Oghalai, "Two-dimensional cochlear micromechanics measured in vivo demonstrate radial tuning within the mouse organ of corti," *Journal of Neuroscience*, vol. 36, no. 31, pp. 8160–8173, 2016.

[52] A. Xia, X. Liu, P. D. Raphael, B. E. Applegate, and J. S. Oghalai, "Hair cell force generation does not amplify or tune vibrations within the chicken basilar papilla," *Nature communications*, vol. 7, p. 13133, 2016.

[53] K. Takada, M. Shimizu, M. Yamada, M. Horiguchi, A. Himeno, and K. Yukimatsu, "Ultrahigh-sensitivity low coherence otdr using er/sup 3+/-doped high-power superfluorescent fibre source," *Electronics Letters*, vol. 28, no. 1, pp. 29–31, 1992.

[54] S. G. Adie, X. Liang, B. F. Kennedy, R. John, D. D. Sampson, and S. A. Boppart, "Spectroscopic optical coherence elastography," *Optics express*, vol. 18, no. 25, pp. 25519–25534, 2010.

[55] J. Zhong, S. Zhong, Q. Zhang, and L. Yao, "Two-dimensional optical coherence tomography for real-time structural dynamical characterization," *Optics and Lasers in Engineering*, vol. 66, pp. 74–79, 2015.